REPORT DOCUMENTATION PAGE	Form Approved OMB NO. 0704-0188

Public reporting burden for this collection of information is estimated to average 1 hour per response, including the time for reviewing instructions, searching existing data sources, gathering and maintaining the data needed, and completing and reviewing the collection of information. Send comment regarding this burden estimates or any other aspect of this collection of information, including suggestions for reducing this burden, to Washington Headquarters Services, Directorate for information Operations and Reports, 1215 Jefferson Davis Highway, Suite 1204, Arlington, VA 22202-4302, and to the Office of Management and Budget, Paperwork Reduction Project (0704-0188), Washington, DC 20503.

1. AGENCY USE ONLY (Leave blank)	2. REPORT DATE Feb. 97	3. REPORT TYPE AND DATES COVERED technical report

4. TITLE AND SUBTITLE	5. FUNDING NUMBERS
A NUMERICAL MODEL FOR BREAKING WAVES: THE VOLUME OF FLUID METHOD	DAAL03-92-G-0116

6. AUTHOR(S)

Philip L.-F. Liu and Pengzhi Lin

7. PERFORMING ORGANIZATION NAMES(S) AND ADDRESS(ES)	8. PERFORMING ORGANIZATION REPORT NUMBER
UNIVERSITY OF DELAWARE CENTER FOR APPLIED COASTAL RESEARCH OCEAN ENGINEERING LABORATORY NEWARK, DE 19716	CACR-97-02

9. SPONSORING / MONITORING AGENCY NAME(S) AND ADDRESS(ES)	10. SPONSORING / MONITORING AGENCY REPORT NUMBER
U.S. Army Research Office P.O. Box 12211 Research Triangle Park, NC 27709-2211	ARO 30379.51-GS-URI

11. SUPPLEMENTARY NOTES

The views, opinions and/or findings contained in this report are those of the author(s) and should not be construed as an official Department of the Army position, policy or decision, unless so designated by other documentation.

12a. DISTRIBUTION / AVAILABILITY STATEMENT	12 b. DISTRIBUTION CODE
Approved for public release; distribution unlimited.	19970321 027

13. ABSTRACT (Maximum 200 words)

This report reviews a numerical model for calculating the evolution of a breaking wave. The model is the combination of a modified version of RIPPLE which was originally developed at Los Alamos National Laboratory (Kothe et al., 1991) and the $k - \epsilon$ turbulence model. In the model, finite difference solutions to the incompressible Reynolds equations for the mean flow field and the $k - \epsilon$ equations for the turbulent field are obtained on a nonuniform mesh. The free surface locations are represented by the volume of fluid (VOF) data on the mesh. A two-step projection method is used for the mean flow solutions, aided by the incomplete Cholesky conjugate gradient technique solving the Poisson equation for the mean pressure field. Advections of momentum in Reynolds equations and turbulent kinetic energy and dissipation rate in the $k - \epsilon$ equations are estimated by the combination of the upwind method and the central difference method. Several numerical examples, including the runup and rundown of nonbreaking and breaking solitary waves, are given. Agreement between the experimental data and the numerical results is very good.

DTIC QUALITY INSPECTED 2

14. SUBJECT

17. SECURITY CLASSIFICATION OR REPORT	18. SECURITY CLASSIFICATION OF THIS PAGE	19. SECURITY CLASSIFICATION OF ABSTRACT	20. LIMITATION OF ABSTRACT
UNCLASSIFIED	UNCLASSIFIED	UNCLASSIFIED	UL

Standard Form 298 (Rev. 2-89)
Prescribed by ANSI Std. 239-18
298-102

A Numerical Model for Breaking Waves: The Volume of Fluid Method

by

Philip L.-F. Liu

and

Pengzhi Lin

CENTER FOR APPLIED COASTAL RESEARCH

Ocean Engineering Laboratory
University of Delaware
Newark, Delaware 19716

A Numerical Model for Breaking Waves: The Volume of Fluid Method

Philip L.-F. Liu and Pengzhi Lin

School of Civil and Environmental Engineering
Cornell University, Ithaca, NY 14853

Abstract

This report reviews a numerical model for calculating the evolution of a breaking wave. The model is the combination of a modified version of RIPPLE which was originally developed at Los Alamos National Laboratory (Kothe et al., 1991) and the $k - \epsilon$ turbulence model. In the model, finite difference solutions to the incompressible Reynolds equations for the mean flow field and the $k - \epsilon$ equations for the turbulent field are obtained on a nonuniform mesh. The free surface locations are represented by the volume of fluid (VOF) data on the mesh. A two-step projection method is used for the mean flow solutions, aided by the incomplete Cholesky conjugate gradient technique solving the Poisson equation for the mean pressure field. Advections of momentum in Reynolds equations and turbulent kinetic energy and dissipation rate in the $k - \epsilon$ equations are estimated by the combination of the upwind method and the central difference method. Several numerical examples, including the runup and rundown of nonbreaking and breaking solitary waves, are given. Agreement between the experimental data and the numerical results is very good.

1   Introduction

Wave transformation phenomena in shallow water are of great theoretical and practical importance. Nearshore breaking waves are central to nearly all coastal processes, including coastal currents and sediment transport. Breaking waves are also responsible for the production of air-bubbles and sea-water droplets, which are important in the consideration of the pollutant transport. From the viewpoint of fluid mechanics, breaking wave transformation processes still possess many challenging but unsolved problems.

Intensive researches have been performed in the last two decades to study the detailed mechanisms of breaking waves. Battjes (1988) summarized both the experimental findings and numerical approaches for the breaking waves in the surf zone. Although many laboratory experiments have been conducted to measure the velocity field and the free-surface profile during the breaking process (e.g. Stive,

1980; Mizuguchi, 1986; Skjelbria, 1987; Nadaoka et al., 1989; Ting and Kirby, 1994, 1995, and 1996), direct numerical solutions for breaking waves are rare. This is primarily due to the lack of understanding of turbulent flows associated with wave breaking.

The early approximation of wave breaking simulation stemmed from the numerical computation of depth averaged equations (DAE), which include both shallow water equations (SWE) and Boussinesq equations (Peregrine, 1967). The energy dissipation due to the breaking process was incorporated into the equations through certain dissipative terms (Abbott et al., 1978; Svendsen et al., 1978). Because the dimension is reduced by one in the DAE, the computational expense is much cheaper than that for full equations and thus this approach can be carried on rather large scale simulation such as tsunami propagation and runup (Liu et al., 1993). Even today, it is still a very active research area of modeling wave transformation in surf zone with the use of the DAE (Abbott et al., 1985; Zelt, 1991; Karambas and Koutitas, 1992; Schäffer et al., 1993; Kobayashi and Karjadi, 1993; Eldeberky and Battjes, 1996). By taking advantage of the simple form of the DAE, however, we should also realize its limitations. Since the DAE approach requires a single value of free surface displacement, this approach cannot predict the detailed configuration of the free surface during the breaking. Furthermore, this approach cannot provide the information of the generation and transport of vorticity and turbulence. These details can only be recovered if the full hydrodynamic equations are solved.

Another important approach to simulate the initiation of wave breaking is to employ the potential flow theory. Before a wave breaks, wave motions are essentially irrotational, except in boundary layer regions. Therefore, the evolution process can be described theoretically by a potential flow theory. The potential flow with a free surface can be numerically computed with the boundary integral equation method (BIEM). The earliest pioneer of using the BIEM to study the wave breaking problem is Longuet-Higgins and Cokelet (1976). The method was further improved by Dommermuth et al. (1988) and Grilli et al. (1994). With the use of the BIEM, the free surface displacement is no longer limited to be single valued as in the DAE. The detailed shape of a curled plunging jet can be simulated very well and the depth-dependent velocity information is also available. However, the BIEM has a severe limitation that the computation cannot continue after the plunging jet touches the front free surface. Therefore, many interesting and important features of wave breaking such as the generation and transport of vorticity and turbulence cannot be studied with the BIEM method.

Free of all the limitations discussed above, the full Reynolds equations can describe the mean (ensemble averaged) motion of any turbulent flow. The Reynolds equations have the similar form as the Navier-Stokes equations (NSE) and the former is actually the special case of the latter when the flow is laminar. The numerical solution to the NSE was studied intensively in 1960's and 1970's. The

earliest solver to the NSE together with the Marker and Cell (MAC) method, a free surface tracking technique, was proposed by Harlow and Welch (1965). The method has been continuously improved in the following decades. One of the outstanding methods is so called the projection method developed by Chorin in 1968 and 1969. This method is very robust and will be adapted in our model, serving as the basic solver to the Reynolds equations.

Another important issue concerning breaking wave computations is the free surface tracking technique. Considering the complex geometry of the free surface during the breaking process, we immediately rule out the traditional height function method that requires the free surface displacement to be single valued. The MAC method (Harlow and Welch, 1965) does not have the limitation of geometry complexity, but it requires too much storage to save the marker information. Because the marker is in general not located at the place where the velocity is defined, the movement of those markers must be based on the interpolated velocity that may lead to rather large accumulated errors. The surface segment method (Miyata, 1986) or the surface marker (SM) method (Chen et al., 1991) significantly reduces the storage by tracking the markers on the free surface only, but it introduces additional difficulties of reordering surface marker when the reconnection of free surface occurs. Such difficulties may becomes unsolvable when a strong breaking takes place that generates many small droplets and bubbles. Attempting to track the density change within each computational cell instead of the free surface location, the volume of fluid (VOF) method (Hirt and Nichols, 1981) provides a robust alternative for updating the free surface. With the considerations of both accuracy and efficiency, we decide to adapt the VOF method in our current model.

Combining the solver to the NSE, such as the projection method, and free surface tracking technique, such as the MAC or the VOF method, we can in principle solve any laminar flow with free surface, i.e., non breaking wave (Chan and Street, 1970). For breaking wave, because of the generation of strong turbulence, additional turbulence model must be added to represent the effect of turbulence on the mean flow motion. In practice, however, the appropriate turbulence models are seldom incorporated into the modeling effort mainly because of the additional difficulties involved. The poor understanding of turbulence characteristics in breaking waves seriously impedes the choice of right turbulence model. For example, Miyata (1986) tried to simulate wave breaking using the surface segment method without including any turbulence model. Wang and Su (1993) also attempted to simulate the wave breaking on sloping beaches using the VOF method without including any turbulence model. In their models, the energy dissipation due to the turbulence is represented by the numerical dissipation partly rather than the appropriate turbulence model. Such simulations do not provide complete information for breaking waves because the important physics of turbulence is not explored in the computation.

In order to account for the turbulence effect on the mean flow, two major tur-

bulence closure models are available which can in principle describe approximately the turbulence generation, transport, and decay. The most complete model is the Reynolds stress closure model, which attempts to close the Reynolds stresses transport equation directly (Launder et al., 1975). Due to the lack of real understanding of turbulence behavior, the closure problem for high order correlation is always a challenging subject. This is especially true for the pressure-strain rate correlation term, which redistributes the turbulence energy among different directions. In fact, based on different assumptions, there are currently at least five different closure models for the pressure-strain rate correlation term and three different models for the diffusion term (Demuren and Sarkar, 1993). The validation and verification of these models for different turbulent flows itself is a very difficult task.

The $k - \epsilon$ model is another important turbulence closure model on the lower level than the Reynolds stress closure model (Launder et al., 1972; Launder and Spalding, 1972; Launder and Spalding, 1974; Rodi, 1980). In this model, instead of seeking the direct closure of the Reynolds stresses transport equations, the eddy-viscosity assumption is made, which relates the Reynolds stresses to k, turbulence kinetic energy, ϵ, the dissipation rate of k, and the rates of strain of the mean flow. The value of k and ϵ can be obtained by solving the transport equations derived from the NSE. The assumption of eddy-viscosity not only reduces the number of transport equations (six for the Reynolds stresses closure model but only one for the k equation) but also simplifies the closure assumption. However, we must realize that such an assumption also limits the application of the model to the nearly isotropically diffusive turbulent flow. At the current stage, we decide to use $k - \epsilon$ model as a preliminary tool. It is our plan to further implement Reynolds stress closure model in the future when more turbulence characteristics in breaking wave is understood through the experimental and numerical studies.

In this report we will review a numerical model which calculates the ensemble averaged flow field. The free surface is tracked with the use of the VOF method. The effects of turbulence are included by coupling the mean momentum equations and the transport equations of turbulence kinetic energy and the dissipation rate. This approach will allow one to examine the free surface configuration, mean velocity and pressure, and the turbulent intensity in broken waves.

2   Mathematical Formulation

In this section, the mathematical equations governing the flow motion and turbulence transport and dissipation will be summarized respectively.

2.1 Flow Motion Formulation

2.1.1 Navier-Stokes Equations and Boundary Conditions

The motions of an incompressible fluid can be described by the Navier-Stokes equations in a bounded domain Ω:

$$\frac{\partial u_i}{\partial x_i} = 0 \tag{1}$$

$$\frac{\partial u_i}{\partial t} + u_j \frac{\partial u_i}{\partial x_j} = -\frac{1}{\rho}\frac{\partial p}{\partial x_i} + g_i + \frac{1}{\rho}\frac{\partial \tau_{ij}}{\partial x_j} \tag{2}$$

where $i, j = 1, 2, 3$ for three-dimensional flows. The Navier-Stokes equations represent the conservation of mass and momentum per unit mass in which u_i denotes the i-th component of the velocity vector, ρ the density, p the pressure, g_i the i-th component of the gravitational acceleration, and τ_{ij} the viscous stress tensor. For a Newtonian fluid, $\tau_{ij} = 2\mu\sigma_{ij}$ with μ being the viscosity and $\sigma_{ij} = \frac{1}{2}(\frac{\partial u_i}{\partial x_j} + \frac{\partial u_j}{\partial x_i})$, the rate of strain tensor. Two types of boundary are considered: rigid boundary Γ_r and free-surface boundary Γ_f. Along the rigid boundary the velocity of the boundary, U_i, is prescribed and the no-slip boundary condition requires

$$u_i = U_i \tag{3}$$

On the free surface the continuity of stress components must be required. Denoting $\mathbf{n}$ as the unit normal on the free surface and n_i as the projection of $\mathbf{n}$ on the x_i, the continuity of the normal stress component can be expressed as

$$p - \mu \left(\frac{\partial u_i}{\partial x_j} + \frac{\partial u_j}{\partial x_i} \right) n_i n_j = \tau_n \tag{4}$$

in which τ_n is a prescribed normal stress applied on the free surface and the surface tension has been ignored. For three-dimensional problems, two unit tangential vectors, $t^k (k = 1, 2)$, are needed to define the local tangent plane on the free surface and t_i^k is defined as the projection of t^k on the x_i. If external tangential stress components are applied on the free surface, τ_t^1 and τ_t^2, the continuity of tangential stress components becomes

$$\mu \left(\frac{\partial u_i}{\partial x_j} + \frac{\partial u_j}{\partial x_i} \right) n_i t_j^k = \tau_t^k \quad , \quad k = 1, 2 \tag{5}$$

In addition to the stress continuity boundary condition on the free surface, which is also referred to as the dynamic free surface boundary condition, the kinematic boundary condition must also be satisfied. Before a wave breaks, such a

boundary condition assumes the velocity continuity that ensures the free surface to be material surface. Since a material surface always consists of the same particles, the total derivative of any physical property associated with the free surface particles, which is expressed as $G(\vec{x}, t)$, must vanish on the free surface. Thus,

$$\frac{\partial G}{\partial t} + u_i \frac{\partial G}{\partial x_i} = 0 \tag{6}$$

After a wave breaks, the free surface is no long a material surface and equation (6) is not valid. In the present model, in conjunction with the volume of fluid method, the G function is chosen as the density function, i.e., $G(\vec{x}, t) = \rho(\vec{x}, t)$. Equation (6) then becomes a generally true statement for an incompressible fluid, before and after the wave breaks. If the density remains a constant, equation (6) is satisfied automatically. However, in the volume of fluid method, the density of a fluid in each computational cell is defined as the averaged density in the cell. Therefore, in the computational cell where the free surface appears, the "density" of the fluid is less than the real density of the fluid, while the "density" of the fluid in the computational cell occupied by air is zero. By tracking the "density" change in each computational cell, one is able to estimate the motion of the free surface.

2.1.2   Reynolds Equations and Boundary Conditions

Equations (1) - (6) describe the governing equation and boundary conditions for a wide range of flow motions of an incompressible fluid with a free surface, including potential flows, laminar and turbulent flows. Once the suitable initial conditions for the velocity and pressure field and the boundary configurations are specified, the formulation is completed. These equations can be solved directly by numerical methods. However, in the case of turbulent flows with high Reynolds number (Re), the resolution for small scale turbulent fluctuations is so high that the direct numerical simulation (DNS) is extremely difficult.

An alternative way to understand turbulent flows is to examine the mean (ensemble averaged) flow field with the consideration of the influence of turbulence. Both the velocity field and the pressure field can be split into mean component and turbulent fluctuations as follows:

$$u_i = \langle u_i \rangle + u_i' \tag{7}$$

$$p = \langle p \rangle + p' \tag{8}$$

$$\frac{1}{\rho} = \frac{1}{\langle \rho \rangle} + \frac{1}{\rho'} \tag{9}$$

in which $\langle \ \rangle$ denotes the mean quantities and the prime "'" represents the turbulent fluctuations. Therefore, $\langle u_i' \rangle = \langle p' \rangle = \langle \frac{1}{\rho'} \rangle = 0$. By substituting (7), (8), and (9)

into (1) and (2) and taking the ensemble average of the resulting equations, one obtains the governing equations for the mean flow field

$$\frac{\partial \langle u_i \rangle}{\partial x_i} = 0 \tag{10}$$

$$\frac{\partial \langle u_i \rangle}{\partial t} + \langle u_j \rangle \frac{\partial \langle u_i \rangle}{\partial x_j} = -\frac{1}{\langle \rho \rangle}\frac{\partial \langle p \rangle}{\partial x_i} + g_i + \frac{1}{\langle \rho \rangle}\frac{\partial \langle \tau_{ij} \rangle}{\partial x_j} - \frac{\partial \langle u_i' u_j' \rangle}{\partial x_j}$$

$$-\langle \frac{1}{\rho'}\frac{\partial p'}{\partial x_i} \rangle + \langle \frac{1}{\rho'}\frac{\partial \tau_{ij}'}{\partial x_j} \rangle \tag{11}$$

These equations are also called the Reynolds equations. It is noted that compared with the classical Reynolds equations, there are two additional terms contributed by the correlations between the density fluctuation and the gradient of pressure fluctuation and viscous stress fluctuation. Since we assume the constant density within the fluid, these two terms only become significant near the free surface. At this time, the importance of these correlations is totally unclear to us and thus we choose to temporarily neglect them in the following computations. Therefore, the only factor that will be taken into account in the mean flow computation is the Reynolds stress,

$$R_{ij} = -\langle \rho \rangle \langle u_i' u_j' \rangle \tag{12}$$

Since all the solid boundary conditions and dynamic free surface boundary conditions are linear in terms of the velocity and pressure, equations (3), (4), and (5) apply also to the mean flow field except that all the instantaneous quantities are replaced by the corresponding ensemble averaged quantities. As for equation (6), since there exist nonlinear terms in the advection of function $G(\vec{x}, t) = \rho$, the additional terms will appear in the mean flow equation. After performing the ensemble average for equation (6) using the similar procedure to that for the mass and momentum conservation equations except for letting $\rho = \langle \rho \rangle + \rho'$, we obtain:

$$\frac{\partial \langle \rho \rangle}{\partial t} + \langle u_i \rangle \frac{\partial \langle \rho \rangle}{\partial x_i} = -\frac{\partial \langle u_i' \rho' \rangle}{\partial x_i} \tag{13}$$

The right hand side of equation (13) represents the correlation between density fluctuations near the free surface and the velocity fluctuations. Again, because of the poor understanding of such correlation, we will temporarily neglect it. Equation (13) becomes the same as equation (6) except that the mean quantities replace the instantaneous quantities.

It is noted that for the turbulent flow, the free surface of the mean flow is no longer clearly defined. The fluctuations of the free surface caused by the velocity

fluctuations in the neighborhood will generate a region with the finite thickness and the variable mean density $\langle \rho \rangle$ that ranges from ρ_f to 0 (air). This region can be regarded as the mean free surface region. The thickness of this region is entirely dependent upon the turbulence intensity.

Realizing the extreme difficulties of the closure problem for the fluctuations of the free surface, we shall neglect this effect by assuming the free surface of the mean flow will be clearly defined even in the turbulent flow, which suggests $\langle \rho \rangle = \rho = \rho_f$ throughout the fluid. Thus, from here on, the $\langle \ \rangle$ sign for the mean density will be dropped. The above approximation enables us to apply the constant density assumption within the well-defined computational domain to simplify the formulation. For example, the viscous term in equation (11) can now be rewritten as $\frac{\partial}{\partial x_j}(2\nu \langle \sigma_{ij} \rangle)$ with $\nu = \mu/\rho$ being the kinematic viscosity. In the following derivation of $k - \epsilon$ model, it is this modified viscous term that will be used rather than the original one in equation (11).

2.2 Turbulence Transport Model

To solve Reynolds equations for the mean flow, one must relate Reynolds stresses to the mean velocity. Extensive research work has been done to seek the proper closure model for the Reynolds stresses in the 1970s (e.g. Launder et al. 1972, 1975). One of the most successful approaches is the $k - \epsilon$ model in which k is the turbulent kinetic energy and ϵ the turbulent dissipation rate, defined as follows

$$k = \frac{1}{2}\langle u_i' u_i' \rangle \quad , \quad \epsilon = \nu \langle \left(\frac{\partial u_i'}{\partial x_j} \right)^2 \rangle \tag{14}$$

The basic concept of the $k - \epsilon$ closure model is to specify the relation between Reynolds stresses and the rates of strain of the mean flow as

$$\langle u_i' u_j' \rangle = -2\nu_t \langle \sigma_{ij} \rangle + \frac{2}{3}k\delta_{ij} \tag{15}$$

in which ν_t is the eddy viscosity, depending on the local state of turbulence, and δ_{ij} is the Kronecker delta. The eddy viscosity is considered as a function of k and ϵ. Therefore, the remaining tasks are: (1) the derivation of governing equations for k and ϵ, and (2) the specification of the relationship among ν_t, k and ϵ.

2.2.1 Transport Equation for Turbulent Kinetic Energy, k

Multiplying the momentum equations for the total velocity (2) by the turbulent velocity component, u_i', and taking the ensemble average of the resulting equations, one obtains a transport equation for the turbulent kinetic energy, k:

$$\frac{\partial k}{\partial t} + \langle u_j \rangle \frac{\partial k}{\partial x_j} = -\frac{1}{\rho}\frac{\partial}{\partial x_j}\left(\langle u_j' p' \rangle + \frac{\rho}{2}\langle u_i'^2 u_j' \rangle \right) + \nu \frac{\partial^2 k}{\partial x_j^2}$$
$$-\langle u_i' u_j' \rangle \frac{\partial \langle u_i \rangle}{\partial x_j} - \nu \langle \left(\frac{\partial u_i'}{\partial x_j} \right)^2 \rangle \qquad (16)$$

The left-hand side of the equation calculates the rate of change of the turbulent kinetic energy following the mean flow field. The first term on the right-hand side represents turbulent diffusion of k through the turbulent pressure work done and the fluxes of kinetic energy. The second term on the right-hand side represents the molecular diffusion of k, which is usually much smaller than the turbulent diffusion. The third term on the right-hand side denotes the rate of change of k due to the working of the Reynolds stresses against the mean flow gradients. Therefore, this term represents the exchanges between the mean flow energy and the turbulent flow energy and it is also called the production term P. The last term in (16) is the energy dissipation rate ϵ caused by the viscous stress.

The governing equation for k as written in (16) still cannot be solved because higher order correlations, $\langle u_j' p \rangle$ and $\langle u_i'^2 u_j' \rangle$, are introduced. In principle one could derive governing equations for these higher order correlations. Unfortunately, even higher correlations will appear in the resulting equations. Certain closure conditions must be imposed to define the problem. Following Launder & Spalding (1972) and Rodi (1980), the turbulent diffusion term in (16) is modeled using a gradient-diffusion hypothesis:

$$-\frac{1}{\rho}\frac{\partial}{\partial x_j}\left(\langle u_j' p \rangle + \frac{\rho}{2}\langle u_i'^2 u_j' \rangle \right) = \frac{\partial}{\partial x_j}\left(\frac{\nu_t}{\sigma_k}\frac{\partial k}{\partial x_j} \right) \qquad (17)$$

in which σ_k is an empirical diffusion constant. Substituting (14), (15) and (17) in (16), one obtains an equation for turbulent kinetic energy, k,

$$\frac{\partial k}{\partial t} + \langle u_j \rangle \frac{\partial k}{\partial x_j} = \frac{\partial}{\partial x_j}\left[\left(\frac{\nu_t}{\sigma_k} + \nu \right) \frac{\partial k}{\partial x_j} \right] + \nu_t \left(\frac{\partial \langle u_i \rangle}{\partial x_j} + \frac{\partial \langle u_j \rangle}{\partial x_i} \right) \frac{\partial \langle u_i \rangle}{\partial x_j} - \epsilon \quad (18)$$

in which the continuity equation for the mean flow, (10), has been employed. To solve the above equation, information on the mean flow field, $\langle u_i \rangle$, which is described by the Reynolds equations, (11), and the turbulent dissipation rate ϵ is required. Therefore, one needs to derive another equation for ϵ.

2.2.2 The Transport Equation for Turbulent Dissipation Rate, ϵ

The ϵ equation can be derived by differentiating the x_i component of the momentum equation (2), multiplying the resulting equation by $\nu \partial u_i'/\partial x_j$, and taking the ensemble average of the resulting equation. Thus,

$$\frac{\partial \epsilon}{\partial t} + \langle u_j \rangle \frac{\partial \epsilon}{\partial x_j} = -2\nu \langle \frac{\partial u_i'}{\partial x_k} \frac{\partial u_i'}{\partial x_j} \frac{\partial u_k'}{\partial x_j} \rangle - 2\langle \left(\nu \frac{\partial^2 u_i'}{\partial x_k \partial x_j} \right)^2 \rangle$$

$$- \frac{1}{\rho} \frac{\partial}{\partial x_k} \left\{ \rho \nu \langle u_k' \left(\frac{\partial u_i'}{\partial x_j} \right)^2 \rangle + 2\nu \langle \frac{\partial u_k'}{\partial x_i} \frac{\partial p'}{\partial x_i} \rangle - \rho \nu \frac{\partial \epsilon}{\partial x_k} \right\}$$

$$- 2\nu \left\{ \langle \frac{\partial u_i'}{\partial x_j} \frac{\partial u_k'}{\partial x_j} \rangle + \langle \frac{\partial u_j'}{\partial x_i} \frac{\partial u_j'}{\partial x_k} \rangle \right\} \frac{\partial \langle u_i \rangle}{\partial x_k} - 2\nu \langle u_k' \frac{\partial u_i'}{\partial x_j} \rangle \frac{\partial^2 \langle u_i \rangle}{\partial x_k \partial x_j} \tag{19}$$

Similar to the exact k-equation, (16), the exact ϵ-equation contains many higher order correlations. The physical meaning of each term on the right-hand side of the equation can be given as follows: The first term represents the production by vortex stretching due to the turbulent vorticity. The second term represents the viscous dissipation due to the spatial gradients of turbulent vorticity. The third term, which is in the form of spatial divergence, represents the molecular and turbulent diffusion of ϵ. The last two terms on the right-hand side of (19) represent the production due to the interaction between turbulent correlations and the mean velocity gradients.

To close the problem the right-hand side terms of (19) will be approximated. First the diffusion terms are modeled by using the gradient-diffusion assumption, i.e.

$$\text{Diffusion of } \epsilon \rightarrow \frac{\partial}{\partial x_j} \left(\frac{\nu_t}{\sigma_\epsilon} \frac{\partial \epsilon}{\partial x_j} \right)$$

where σ_ϵ is an empirical constant. Secondly, the difference between the production and dissipation will be modeled as (Rodi 1980)

$$\text{(Production - Dissipation)}_\epsilon \rightarrow C_{1\epsilon} \frac{\epsilon}{k} \nu_t \left(\frac{\partial \langle u_i \rangle}{\partial x_j} + \frac{\partial \langle u_j \rangle}{\partial x_i} \right) \frac{\partial \langle u_i \rangle}{\partial x_j} - C_{2\epsilon} \frac{\epsilon^2}{k}$$

in which $C_{1\epsilon}$ and $C_{2\epsilon}$ are two more empirical coefficients related to production and dissipation of ϵ, respectively. It is also noted that the k/ϵ denotes the characteristic decay time. Equation (19) can now be simplified to be

$$\frac{\partial \epsilon}{\partial t} + \langle u_j \rangle \frac{\partial \epsilon}{\partial x_j} = \frac{\partial}{\partial x_j} \left(\frac{\nu_t}{\sigma_\epsilon} \frac{\partial \epsilon}{\partial x_j} \right) + C_{1\epsilon} \frac{\epsilon}{k} \nu_t \left(\frac{\partial \langle u_i \rangle}{\partial x_j} + \frac{\partial \langle u_j \rangle}{\partial x_i} \right) \frac{\partial \langle u_i \rangle}{\partial x_j} - C_{2\epsilon} \frac{\epsilon^2}{k} \tag{20}$$

From the dimensional analysis, the eddy viscosity has a unit of (length^2/time). Thus, an empirical relation among ν_t, k and ϵ can be written as

$$\nu_t = C_d \frac{k^2}{\epsilon} \tag{21}$$

where C_d is an empirical constant.

Although the closure assumptions employed in the $k - \epsilon$ equations are crude, this model has been successfully used to predict many complex flows. The empirical coefficients appeared in the model are surprisingly universal. The recommended values for these coefficients are (Rodi 1980):

$$C_d = 0.09, \quad C_{1\epsilon} = 1.44, \quad C_{2\epsilon} = 1.92, \quad \sigma_k = 1.0, \quad \sigma_\epsilon = 1.3 \tag{22}$$

2.2.3 Determinations of the coefficients in $k - \epsilon$ model

Although the coefficients for the $k - \epsilon$ model are somehow regarded to be standard for many types of turbulent flows, it is still worthwhile to know how these coefficients have been determined and what assumptions have been made. These assumptions also suggest the limitations of the model and the possibilities for further improvement.

It is realized that the original $k - \epsilon$ equations are derived from the basic flow motion equations, i.e., Navier-Stokes equations and Reynolds stresses equations, with no additional assumptions. The $k - \epsilon$ model, however, consists of a lot assumptions in order to close the high order correlations. Besides those assumptions in the turbulence model, we also assume that the fundamental turbulence characteristics does not change under different flow fields. For example, we assume that the same $k - \epsilon$ model with the same coefficients should apply equally to both well-developed turbulent flows and transient turbulent flows. The major reason to make such assumption is that many turbulence measurements that are used to estimate the model parameters can only be performed and analyzed under simple and quasi-steady state (well-developed turbulence). While most engineering applications of turbulent flows are complicated and transient. The gap between the theoretical study of a simple turbulent flow and the practical application of the complicated turbulent flows has not been resolved. In our study, we retain the above assumption to study the complicated and transient turbulent flow with the use of turbulence model whose coefficients are essentially determined under the simple situations.

2.2.3.1 Determination of $C_{2\epsilon}$

To determine $C_{2\epsilon}$, we will consider the simple dissipative turbulent flow. In such flow, there is no mean velocity gradient and thus there is no turbulence production. The typical example is one-dimensional grid turbulence in x direction that is created by making flow pass certain grid system. If the advection is much

stronger than diffusion. $C_{2\epsilon}$ would be the only coefficient appearing in equations (18) and (20). For the well developed turbulence, we also neglect the time derivative term so that k and ϵ are functions of x only. The simplified equations read:

$$\langle u \rangle \frac{dk}{dx} = -\epsilon \tag{23}$$

$$\langle u \rangle \frac{d\epsilon}{dx} = -C_{2\epsilon} \frac{\epsilon^2}{k} \tag{24}$$

The general solution for above equations system are:

$$k = k_0 (1 + \xi x)^{-n} \tag{25}$$

$$\epsilon = \epsilon_0 (1 + \xi x)^{-n-1} \tag{26}$$

with ξ and n coefficients and

$$C_{2\epsilon} = \frac{n+1}{n} \tag{27}$$

The measurement of the decay rate of k in the grid turbulence, $-n$, indicates that $C_{2\epsilon}$ lies in the range of 1.8 and 2.0 (Rodi, 1980). In most models, $C_{2\epsilon}$ is selected to be 1.9.

2.2.3.2 Determination of C_d

Next, we turn to estimate the value of C_d, the coefficient that relates the value of k and ϵ to eddy viscosity ν_t. For local equilibrium shear layers that generally exist in constant-stress turbulent boundary layers, $P = \epsilon$. Because in the shear layer, $P = \nu_t (\frac{\partial \langle u \rangle}{\partial y})^2 = \frac{(\langle u'v' \rangle)^2}{\nu_t}$, where y is the coordinate normal to the mean flow $\langle u \rangle$, and according to the definition, $\epsilon = C_d \frac{k^2}{\nu_t}$, we have:

$$C_d = \left(\frac{\langle u'v' \rangle}{k} \right)^2 \tag{28}$$

According to the measurements, the value of $\frac{\langle u'v' \rangle}{k}$ in such flows is around 0.3 that gives $C_d = 0.09$.

2.2.3.3 Determination of $C_{1\epsilon}$

In the log-law region of a fully developed turbulent channel flow, it is assumed that $P \approx \epsilon$ and all the advection is negligible. The mean velocity gradient can be expressed as $\frac{\partial \langle u \rangle}{\partial y} = \frac{u_*}{\kappa y}$ with y again being the coordinate normal to the mean flow

12

direction, $u_* = \sqrt{\tau_w/\rho}$ being the frictional velocity, and $\kappa = 0.41$ being the von Karman constant. τ_w is the cross-stream shear stress on the wall. It is ready to show that in such a log-law region, the k remains constant over y, $k = \frac{u_*^2}{\sqrt{C_d}}$, $\epsilon = \frac{u_*^3}{\kappa y}$, and $u_*^2 = -\langle u'v' \rangle$. We will discuss this in more detail later when we propose the wall boundary condition for the $k - \epsilon$ model. With all the assumptions mentioned above, the equation for ϵ (20) can be reduced to:

$$\frac{C_d k^2}{\sigma_\epsilon \epsilon} \frac{d^2 \epsilon}{dy^2} - \frac{C_d k^2}{\sigma_\epsilon \epsilon^2} \left(\frac{d\epsilon}{dy}\right)^2 + (C_{1\epsilon} - C_{2\epsilon}) \frac{\epsilon^2}{k} = 0 \tag{29}$$

By substituting the solution form for ϵ into the above equation, we obtain:

$$C_{1\epsilon} = C_{2\epsilon} - \frac{\kappa^2}{\sigma_\epsilon \sqrt{C_d}} \tag{30}$$

As long as the coefficient C_d, $C_{2\epsilon}$, and σ_ϵ are known, the value of $C_{1\epsilon}$ is fixed. At this time, we have already determined the value of C_d and $C_{2\epsilon}$, the remaining task is then to determine the value of σ_ϵ so that we can estimate $C_{1\epsilon}$.

2.2.3.4 Determinations of σ_ϵ and σ_k

It is expected that the value of σ_ϵ and σ_k are close to unity that implies that both k and ϵ diffuse at roughly the same rate as the mean velocity. By the computer optimization (Launder et al., 1972), the value of σ_ϵ and σ_k are chosen to be 1.3 and 1.0, respectively. The value of σ_ϵ fixes the value of $C_{1\epsilon}$ to be 1.49. However, in most applications of the $k - \epsilon$ model, this coefficient is adapted as 1.44 as first appearing in Launder and Spalding (1974).

2.2.4 Boundary Conditions for k and ϵ

Although the boundary conditions for the total flow field along the solid boundaries and the free surface have been described in (3), (4), and (5), additional boundary conditions must be given in terms of k and ϵ. Since the physics of breaking waves are not well understood, especially near the free surface, it is extremely difficult to prescribe boundary conditions for k and ϵ. For the situations where the external forces are absent on the free surface it seems to be reasonable to assume that turbulence does not diffuse across the free surface. Consequently, the normal flux of k and ϵ should vanish on the free surface,

$$\frac{\partial k}{\partial x_i} n_i = 0 \quad , \quad \frac{\partial \epsilon}{\partial x_i} n_i = 0 \tag{31}$$

In theory, the turbulence vanishes at wall which dictates that both k and ϵ become zero at wall. However, in most of practical computations, the resolution

13

cannot be so small to resolve the viscous sublayer. Thus, the boundary conditions for k and ϵ are generally specified in the turbulent boundary layer instead of right on the wall. In the turbulent boundary layer the cross-stream shear stress dominates and remains a constant. Invoking the boundary layer approximation, we have:

$$-\frac{\langle u'v' \rangle}{\partial y} + \nu \frac{\partial^2 \langle u \rangle}{\partial y^2} = 0 \tag{32}$$

where y is the coordinate normal to the wall. By taking the integration from the wall to the place out of the viscous layer where the viscous effect can be neglected, we have:

$$-\langle u'v' \rangle |_{y=y} = -\nu \frac{\partial \langle u \rangle}{\partial y}\Big|_{y=0} = \frac{1}{\rho}\tau_w = u_*^2 \tag{33}$$

As discussed in section 2.2.3.3, the mean velocity gradient in this region can be expressed as:

$$\frac{d\langle u \rangle}{dy} = \frac{u_*}{\kappa y} \tag{34}$$

Integrating the above equation, we have so called logarithmic-law profile for streamwise velocity:

$$\frac{\langle u \rangle}{u_*} = \frac{1}{\kappa}\ell n\left(E\frac{u_* y}{\nu}\right) \tag{35}$$

where $E = 9.0$ for a smooth wall. Because the dissipation rate is approximately the same as production rate, $\epsilon = P$, from (33) and (34) we have:

$$\epsilon = -\langle u'v' \rangle \frac{d\langle u \rangle}{dy} = \frac{u_*^3}{\kappa y} \tag{36}$$

From (15) the eddy viscosity ν_t can be obtained

$$\nu_t = -\frac{\langle u'v' \rangle}{\frac{\partial \langle u \rangle}{\partial y}} = \kappa u_* y \tag{37}$$

Namely, the eddy viscosity is proportional to the distance from the wall in the turbulent boundary layer. Substituting (36) and (37) into (21) yields

14

$$k = \frac{u_*^2}{\sqrt{C_d}} \tag{38}$$

Equations (36) and (38) constitute the boundary conditions for k and ϵ at the computational points immediately adjacent to the solid boundary. The frictional velocity can be found from (35) once the velocity field has been calculated.

2.3 Summary of Governing Equations

Before we leave this section, it is useful to have a brief summary of the assumptions made so far in deriving the Reynolds equations for mean flow motions and the $k - \epsilon$ model for turbulence transport. The final formula that will be used in the later numerical model will also be presented. Since only the mean quantities are involved in the Reynolds equations and $k - \epsilon$ model, the symbol for the ensemble average, $\langle \ \rangle$, will be dropped from herein for simplicity. By invoking the eddy viscosity assumption (15) and neglecting density fluctuations near free surface, equations (10) and (11) that governing the mass and momentum conservation of mean flow can be rewritten as:

$$\frac{\partial u_i}{\partial x_i} = 0 \tag{39}$$

$$\frac{\partial u_i}{\partial t} + u_j \frac{\partial u_i}{\partial x_j} = -\frac{1}{\rho} \frac{\partial p}{\partial x_i} + g_i + \frac{\partial \tau_{ij}}{\partial x_j} \tag{40}$$

The density change equation that can be used to track the free surface is written as:

$$\frac{\partial \rho}{\partial t} + u_i \frac{\partial \rho}{\partial x_i} = 0 \tag{41}$$

The $k - \epsilon$ model reads:

$$\frac{\partial k}{\partial t} + u_j \frac{\partial k}{\partial x_j} = \frac{\partial}{\partial x_j}\left[(\frac{\nu_t}{\sigma_k} + \nu)\frac{\partial k}{\partial x_j}\right] + 2\nu_t \sigma_{ij}\frac{\partial u_i}{\partial x_j} - \epsilon \tag{42}$$

$$\frac{\partial \epsilon}{\partial t} + u_j \frac{\partial \epsilon}{\partial x_j} = \frac{\partial}{\partial x_j}\left[(\frac{\nu_t}{\sigma_\epsilon} + \nu)\frac{\partial \epsilon}{\partial x_j}\right] + C_{1\epsilon}\frac{\epsilon}{k}2\nu_t \sigma_{ij}\frac{\partial u_i}{\partial x_j} - C_{2\epsilon}\frac{\epsilon^2}{k} \tag{43}$$

and the total stresses τ_{ij} in equation (40) is related to k, ϵ, and σ_{ij} in the following way,

$$\tau_{ij} = 2(\nu + C_d\frac{k^2}{\epsilon})\sigma_{ij} - \frac{2}{3}k\delta_{ij}$$

Equations (39) to (43) will serve as the governing equations to be solved numerically.

15

3   Numerical Model

In this section, we will review the numerical methods used to solve the turbulent flow problem as described in the previous section. Currently, we will restrict ourselves to the two-dimensional problems only.

3.1   Schematics of Computational Domain

The finite difference method will be used throughout the computation. At the beginning, the whole computational domain is discretized by the $m \times n$ rectangular cells as sketched in figure 1. All scalar quantities, i.e., p, k, ϵ, the volume of fluid (VOF) function F, and the openness function θ_c, are defined in the center of the cells. The first three scalars have been introduced before, and the last two scalars will be defined later. The vector and vector-related quantities, i.e., the x- and y-components of the mean velocities, u, v, and the openness functions on the cell faces, θ_r and θ_t, are defined in the cell faces as shown in figure 1. Again, the last two functions will be defined in the following text.

As mentioned before, the exact location of the free surface will not be pursuited in the present model. Instead, the density change in each cell will be tracked so that the location of the free surface can be identified. We assume that the density is a constant ρ_f for the fluid, and the averaged density in the cell is defined as, $\rho = \frac{\rho_f V_f}{V_f + V_a}$, where V_f is the volume of the fluid in the cell and V_a is the volume of the air in the cell. Before solving the density change equation (41), we further simplify the problem by using the normalized averaged density or the VOF function, $F = \rho/\rho_f$. With the aid of the VOF function, we may identify the cell types readily. For example, the empty (E) cell is defined as the cell with $F = 0$, where the computation will be skipped; the surface (S) cell is defined as the cell with $F > 0$ and adjacent to at least one empty cell, where the free surface boundary condition will be applied; and the interior (I) cell is defined as the cell which has no empty neighbour cells, where the main computation will be conducted.

Another important issue is how to represent the arbitrary shape of solid boundary. In other models, the solid boundary is generally redefined as sawtooth-shape surface to fit the cell boundary (Lemos, 1992). Based on our numerical tests, such a treatment may generate the significant spurious reflection during the wave shoaling. In the current model, the more flexible way to represent the solid boundary, partial cell treatment, is adapted. In such treatment, the solid object is modeled as the special case of the two-phase flow with infinite density. The openness functions are introduced at the cell itself and on the cell faces. At the cell center, θ_c is defined as the ratio of space not occupied by the solid object (thus open to the fluid) to the whole cell area. On the cell faces, θ_r (θ_t) is defined as the length open to the fluid to the whole length of the right (top) cell boundary. Therefore, similar to the VOF function, the openness functions can provide the information whether
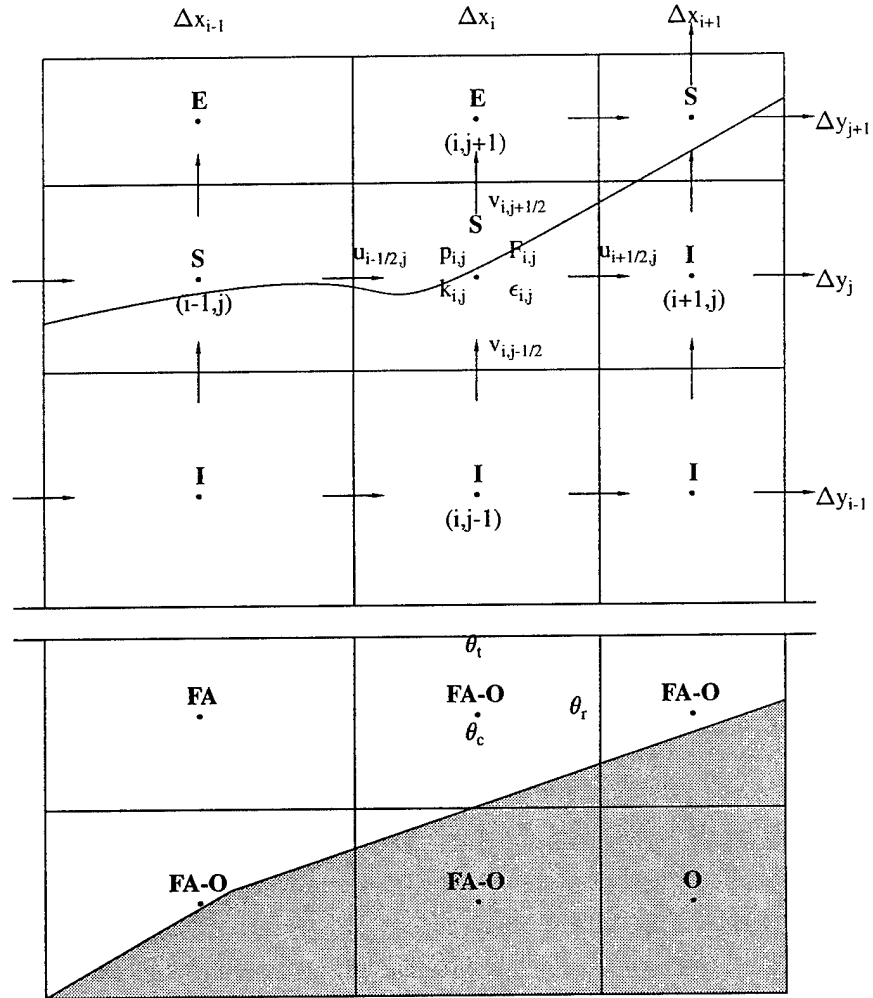
Figure 1: Finite difference meshes and cell classifications in the model

the cell is the solid object or obstacle (O), the fluid (air)-solid boundary (FA-O), or the fluid (air) domain (FA). The only difference between the VOF function and the openness functions is that the former is a time-varying function and the latter are not.

Figure 1 illustrates the definition of different cell types based on the information of the VOF function and openness functions. In the following context, the implementation of the VOF function advection and the treatment of solid boundary with openness functions will be discussed in more detail.

3.2   Two-step Projection Method

The two-step projection method (Chorin 1968, 1969) has been used to solve the Reynolds equations. The first step is to introduce an intermediate velocity $\tilde{u}_i$, which carries the correct vorticity, as

$$\frac{\tilde{u}_i^{n+1} - u_i^n}{\Delta t} = -u_j^n \frac{\partial u_j^n}{\partial x_j} + g_i + \frac{\partial \tau_{ij}^n}{\partial x_j} \tag{44}$$

in which the superscript indicates the time level and Δt is the time step size. The subscripts $i, j = 1, 2$ for two-dimensional problems, i.e., $u_1 = u$, $u_2 = v$, $x_1 = x$, and $y_1 = y$. Therefore (44) is the forward time difference equation of the Reynolds equation without the pressure gradient term. The intermediate velocity $\tilde{u}_i$ does not, in general, satisfy the continuity equation. If all information on the n-th time level is known, (44) is an explicit formula for $\tilde{u}_i^{n+1}$.

The second step is to project the intermediate velocity field onto a divergence-free plane to obtain the final velocity:

$$\frac{u_i^{n+1} - \tilde{u}_i^{n+1}}{\Delta t} = -\frac{1}{\rho^n} \frac{\partial p^{n+1}}{\partial x_i} \tag{45}$$

$$\frac{\partial u_i^{n+1}}{\partial x_i} = 0 \tag{46}$$

One can combine (44) and (45) to show that the Reynolds equations are satisfied approximately, with pressure gradient being evaluated at the $(n+1)$-th time level. The continuity equation is satisfied by (46). Taking the divergence of (45) and applying (46) to the resulting equation yields

$$\frac{\partial}{\partial x_i} \left(\frac{1}{\rho^n} \frac{\partial p^{n+1}}{\partial x_i} \right) = \frac{1}{\Delta t} \frac{\partial \tilde{u}_i^{n+1}}{\partial x_i} \tag{47}$$

which is also called the Poisson Pressure Equation (PPE).

18

3.3 Spatial Discretization in Finite Difference Form

In the two-step projection method the spatial derivations of the velocity components and the pressure field need to be expressed in finite-difference forms. As discussed before and shown in figure 1, the present scheme calculates the velocity components, u and v, on the vertical and horizontal cell faces, respectively. The pressure and other scalars such as k, ϵ, and the volume of fluid function F are defined at the cell center. It is noted that in the finite difference form, some variables are needed at the place where they are not originally defined. For instance, u at the horizontal cell face and v at the vertical cell face. In such circumstances, the linear interpolation will be used. The most commonly used interpolated variables are given as follows:

$$u_{i,j} = \frac{1}{2}(u_{i+\frac{1}{2},j} + u_{i-\frac{1}{2},j}) \tag{48}$$

$$v_{i,j} = \frac{1}{2}(v_{i,j+\frac{1}{2}} + v_{i,j-\frac{1}{2}}) \tag{49}$$

$$u_{i,j+\frac{1}{2}} = \frac{u_{i,j+1}\Delta y_j + u_{i,j}\Delta y_{j+1}}{\Delta y_j + \Delta_{j+1}} \tag{50}$$

$$v_{i+\frac{1}{2},j} = \frac{v_{i+1,j}\Delta x_i + v_{i,j}\Delta x_{i+1}}{\Delta x_i + \Delta x_{i+1}} \tag{51}$$

$$\Delta x_{i+\frac{1}{2}} = \frac{1}{2}(\Delta x_i + \Delta x_{i+1}) \tag{52}$$

$$\Delta y_{j+\frac{1}{2}} = \frac{1}{2}(\Delta y_j + \Delta y_{j+1}) \tag{53}$$

As appearing in equation (44), all the advection terms and diffusion terms will be evaluated at the n-th time step. The advection terms in the x-momentum equation $u\frac{\partial u}{\partial x} + v\frac{\partial u}{\partial y}$ are evaluated at the front (right) face of the cell. The advection terms in the y-momentum equation $u\frac{\partial v}{\partial x} + v\frac{\partial v}{\partial y}$, are calculated at the top face of the cell (Figure 2). Thus

$$u\frac{\partial u}{\partial x} + v\frac{\partial u}{\partial y} = u_{i+\frac{1}{2},j}\left(\frac{\partial u}{\partial x}\right)_{i+\frac{1}{2},j} + v_{i+\frac{1}{2},j}\left(\frac{\partial u}{\partial y}\right)_{i+\frac{1}{2},j} \tag{54}$$

$$u\frac{\partial v}{\partial x} + v\frac{\partial v}{\partial y} = u_{i,j+\frac{1}{2}}\left(\frac{\partial v}{\partial x}\right)_{i,j+\frac{1}{2}} + v_{i,j+\frac{1}{2}}\left(\frac{\partial v}{\partial y}\right)_{i,j+\frac{1}{2}} \tag{55}$$

In equation (54) one needs to specify the spatial derivatives of the horizontal velocity. To calculate these spatial derivations of the horizontal velocity component in (54), one can use the combination of the upwind scheme and the central difference scheme. For instance
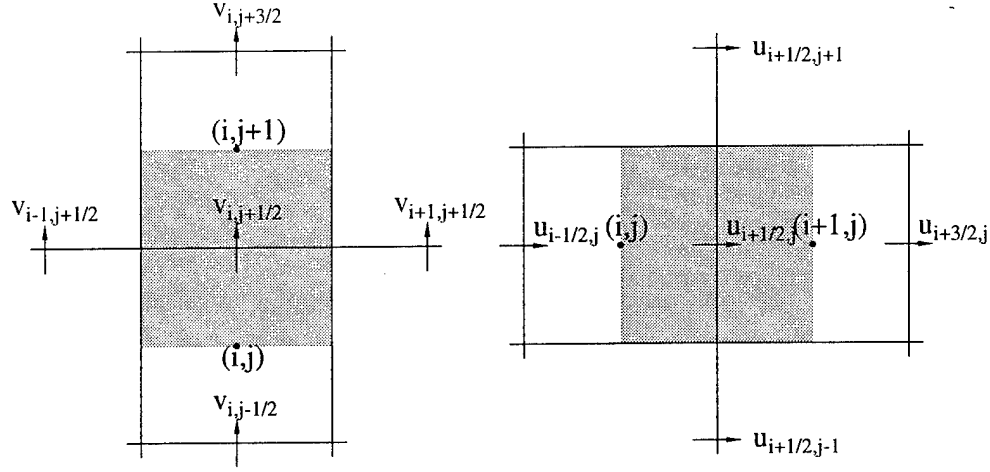
Figure 2: Momentum control volume for x and y advections

$$\left(\frac{\partial u}{\partial x}\right)_{i+\frac{1}{2},j} = \begin{cases} \left(\frac{\partial u}{\partial x}\right)_{i,j} & , \quad \text{if } u_{i+\frac{1}{2},j} > 0 \\ \left(\frac{\partial u}{\partial x}\right)_{i+1,j} & , \quad \text{if } u_{i+\frac{1}{2},j} < 0 \end{cases} \tag{56}$$

for the upwind scheme. On the other hand

$$\left(\frac{\partial u}{\partial x}\right)_{i+\frac{1}{2},j} = \frac{\Delta x_{i+1}\left(\frac{\partial u}{\partial x}\right)_{i,j} + \Delta x_i \left(\frac{\partial u}{\partial x}\right)_{i+1,j}}{\Delta x_i + \Delta x_{i+1}} \tag{57}$$

for the central difference scheme. In both (56) and (57)

$$\left(\frac{\partial u}{\partial x}\right)_{i,j} = \frac{u_{i+\frac{1}{2},j} - u_{i-\frac{1}{2},j}}{\Delta x_i} \tag{58a}$$

$$\left(\frac{\partial u}{\partial x}\right)_{i+1,j} = \frac{u_{i+\frac{3}{2},j} - u_{i+\frac{1}{2},j}}{\Delta x_{i+1}} \tag{58b}$$

are defined. Since the upwind scheme usually introduce significant numerical damping and the central difference scheme generates numerical instability, a combination of these two schemes usually yield a more accurate numerical solution. Thus, the general formula for the spatial derivative becomes

20

$$\left(\frac{\partial u}{\partial x}\right)_{i+\frac{1}{2},j} = \left\{\left[1 + \alpha \, sgn\left(u_{i+\frac{1}{2},j}\right)\right]\Delta x_{i+1}\left(\frac{\partial u}{\partial x}\right)_{i,j}\right.$$
$$\left. + \left[1 - \alpha \, sgn\left(u_{i+\frac{1}{2},j}\right)\right]\Delta x_i\left(\frac{\partial u}{\partial x}\right)_{i+1,j}\right\}/\Delta x_\alpha \tag{59}$$

where

$$\Delta x_\alpha = \Delta x_{i+1} + \Delta x_i + \alpha \, sgn\left(u_{i+\frac{1}{2},j}\right)\left(\Delta x_{i+1} - \Delta x_i\right) \tag{60}$$

Similarly

$$\left(\frac{\partial u}{\partial y}\right)_{i+\frac{1}{2},j} = \left\{\left[1 + \alpha \, sgn\left(v_{i+\frac{1}{2},j}\right)\right]\Delta y_{j+\frac{1}{2}}\left(\frac{\partial u}{\partial y}\right)_{i+\frac{1}{2},j-\frac{1}{2}}\right.$$
$$\left. + \left[1 - \alpha \, sgn\left(v_{i+\frac{1}{2},j}\right)\right]\Delta y_{j-\frac{1}{2}}\left(\frac{\partial u}{\partial y}\right)_{i+\frac{1}{2},j+\frac{1}{2}}\right\}/\Delta y_\alpha \tag{61}$$

where

$$\Delta y_\alpha = \Delta y_{j+\frac{1}{2}} + \Delta y_{j-\frac{1}{2}} + \alpha \, sgn\left(v_{i+\frac{1}{2},j}\right)\left(\Delta y_{j+\frac{1}{2}} - \Delta y_{j-\frac{1}{2}}\right) \tag{62}$$
$$\tag{63}$$

and

$$\left(\frac{\partial u}{\partial y}\right)_{i+\frac{1}{2},j+\frac{1}{2}} = \frac{u_{i+\frac{1}{2},j+1} - u_{i+\frac{1}{2},j}}{\Delta y_{j+\frac{1}{2}}} \tag{64a}$$

$$\left(\frac{\partial u}{\partial y}\right)_{i+\frac{1}{2},j-\frac{1}{2}} = \frac{u_{i+\frac{1}{2},j} - u_{i+\frac{1}{2},j-1}}{\Delta y_{j-\frac{1}{2}}} \tag{64b}$$

In the above equations, the coefficient α is the weighting factor between the upwind method and the central difference method. When $\alpha = 0$, the finite difference form becomes the central difference, while $\alpha = 1$, the finite difference form becomes the upwind difference. In practice, α is generally selected in the range of 0.3 to 0.5 to produce the stable and accurate results. The finite difference form for the advection terms in the y-momentum equation (55) can be similarly obtained.

After neglecting the term $-\frac{2}{3}k\delta_{ij}$ in the total stresses, which can be lumped into the pressure term, the gradients of the total stresses in (44) can be represented by the diffusion terms that are written as

21

$$\frac{\partial}{\partial x}\left[2\left(\nu+\nu_t\right)\frac{\partial u}{\partial x}\right] + \frac{\partial}{\partial y}\left[\left(\nu+\nu_t\right)\left(\frac{\partial u}{\partial y}+\frac{\partial v}{\partial x}\right)\right] \tag{65}$$

for the x-momentum equation and

$$\frac{\partial}{\partial x}\left[\left(\nu+\nu_t\right)\left(\frac{\partial v}{\partial x}+\frac{\partial u}{\partial y}\right)\right] + \frac{\partial}{\partial y}\left[2\left(\nu+\nu_t\right)\frac{\partial v}{\partial y}\right] \tag{66}$$

for the y-momentum equation. Once again the diffusion of the momentum in the x-direction is calculated at the right face of the computational cell, while the diffusion in the y-direction is computed at the top face of the cell. The central differencing method is used to express the derivatives. Thus, the first term of (65) can be written in the following finite differences from

$$\left\{\frac{\partial}{\partial x}\left[2\left(\nu+\nu_t\right)\frac{\partial u}{\partial x}\right]\right\}_{i+\frac{1}{2},j} = 2\frac{\left(\nu+\nu_t\right)_{i+1,j}\left(\frac{\partial u}{\partial x}\right)_{i+1,j} - \left(\nu+\nu_t\right)_{i,j}\left(\frac{\partial u}{\partial x}\right)_{i,j}}{\Delta x_{i+\frac{1}{2}}}$$

$$= \frac{2}{\Delta x_{i+\frac{1}{2}}}\left[\left(\nu+\nu_t\right)_{i+1,j}\frac{u_{i+\frac{3}{2},j}-u_{i+\frac{1}{2},j}}{\Delta x_{i+1}} - \left(\nu+\nu_t\right)_{i,j}\frac{u_{i+\frac{1}{2},j}-u_{i-\frac{1}{2},j}}{\Delta x_i}\right] \tag{67a}$$

The second term in (65) can be written as

$$\left\{\frac{\partial}{\partial y}\left[\left(\nu+\nu_t\right)\left(\frac{\partial u}{\partial y}+\frac{\partial v}{\partial x}\right)\right]\right\}_{i+\frac{1}{2},j} = \frac{1}{\Delta y_j}\left\{\left(\nu+\nu_t\right)_{i+\frac{1}{2},j+\frac{1}{2}}\left(\frac{\partial u}{\partial y}+\frac{\partial v}{\partial x}\right)_{i+\frac{1}{2},j+\frac{1}{2}}\right.$$

$$\left. \left(-\nu+\nu_t\right)_{i+\frac{1}{2},j-\frac{1}{2}}\left(\frac{\partial u}{\partial y}+\frac{\partial v}{\partial x}\right)_{i+\frac{1}{2},j-\frac{1}{2}}\right\} \tag{67b}$$

in which

$$\left(\frac{\partial u}{\partial y}+\frac{\partial v}{\partial x}\right)_{i+\frac{1}{2},j+\frac{1}{2}} = \frac{u_{i+\frac{1}{2},j+1}-u_{i+\frac{1}{2},j}}{\Delta y_{j+\frac{1}{2}}} + \frac{v_{i+1,j+\frac{1}{2}}-v_{i,j+\frac{1}{2}}}{\Delta x_{i+\frac{1}{2}}} \tag{68a}$$

and

$$\left(\frac{\partial u}{\partial y}+\frac{\partial v}{\partial x}\right)_{i+\frac{1}{2},j-\frac{1}{2}} = \frac{u_{i+\frac{1}{2},j}-u_{i+\frac{1}{2},j-1}}{\Delta y_{j-\frac{1}{2}}} + \frac{v_{i+1,j-\frac{1}{2}}-v_{i,j-\frac{1}{2}}}{\Delta x_{i+\frac{1}{2}}} \tag{68b}$$

Similar finite-difference formulas can be obtained for the diffusion terms in the y-momentum equation (66).

In the second step of the projection method, the Poisson Pressure equation (47) needs to be solved. In the two-dimensional form (47) can be rewritten as

$$\frac{\partial}{\partial x}\left(\frac{1}{\rho^n}\frac{\partial p^{n+1}}{\partial x}\right) + \frac{\partial}{\partial y}\left(\frac{1}{\rho^n}\frac{\partial p^{n+1}}{\partial y}\right) = \frac{1}{\Delta t}\left(\frac{\partial \tilde{u}}{\partial x} + \frac{\partial \tilde{v}}{\partial y}\right) \tag{69}$$

Since the pressure is evaluated at the center of the computational cell, the Poisson equation is also evaluated at the center. Thus, the left-hand side of the equation can be expressed as:

$$\left\{\frac{\partial}{\partial x}\left(\frac{1}{\rho^n}\frac{\partial p^{n+1}}{\partial x}\right)\right\}_{i,j} = \frac{1}{\Delta x_i}\left\{\frac{1}{\rho^n_{i+\frac{1}{2},j}}\left(\frac{\partial p}{\partial x}\right)^{n+1}_{i+\frac{1}{2},j} - \frac{1}{\rho^n_{i-\frac{1}{2},j}}\left(\frac{\partial p}{\partial x}\right)^{n+1}_{i-\frac{1}{2},j}\right\}$$

$$= \frac{1}{\Delta x_i}\left\{\frac{1}{\rho^n_{i+\frac{1}{2},j}}\left(\frac{p^{n+1}_{i+1,j} - p^{n+1}_{i,j}}{\Delta x_{i+\frac{1}{2}}}\right) - \frac{1}{\rho_{i-\frac{1}{2}}{}^n{}_{,j}}\left(\frac{p^{n+1}_{i,j} - p^{n+1}_{i-1,j}}{\Delta x_{i-\frac{1}{2}}}\right)\right\} \tag{70a}$$

$$\left\{\frac{\partial}{\partial y}\left(\frac{1}{\rho^n}\frac{\partial p^{n+1}}{\partial y}\right)\right\}_{i,j} = \frac{1}{\Delta y_i}\left\{\frac{1}{\rho^n_{i,j+\frac{1}{2}}}\left(\frac{\partial p}{\partial y}\right)^{n+1}_{i,j+\frac{1}{2}} - \frac{1}{\rho^n_{i,j-\frac{1}{2}}}\left(\frac{\partial p}{\partial y}\right)^{n+1}_{i,j-\frac{1}{2}}\right\}$$

$$= \frac{1}{\Delta y_i}\left\{\frac{1}{\rho^n_{i,j+\frac{1}{2}}}\left(\frac{p^{n+1}_{i,j+1} - p^{n+1}_{i,j}}{\Delta y_{j+\frac{1}{2}}}\right) - \frac{1}{\rho^n_{i,j-\frac{1}{2}}}\left(\frac{p^{n+1}_{i,j} - p^{n+1}_{i,j-1}}{\Delta y_{j-\frac{1}{2}}}\right)\right\} \tag{70b}$$

The right-hand side of (69) is expressed as

$$\left(\frac{\partial \tilde{u}}{\partial x} + \frac{\partial \tilde{v}}{\partial y}\right)_{i,j} = \frac{\tilde{u}_{i+\frac{1}{2},j} - \tilde{u}_{i-\frac{1}{2},j}}{\Delta x_i} + \frac{\tilde{v}_{i,j+\frac{1}{2}} - \tilde{v}_{i,j-\frac{1}{2}}}{\Delta y_j} \tag{70c}$$

which are the known quantities. In (70a) and (70b) the density on the side of the cells can be obtained by the linear interpolation, i.e.

$$\rho^n_{i+\frac{1}{2},j} = \frac{\rho^n_{i,j}\Delta x_{i+1} + \rho^n_{i+1,j}\Delta x_i}{\Delta x_i + \Delta x_{i+1}} \tag{71}$$

Substituting (70) and (71) into the Poisson equation yields a set of linear algebraic equations for the pressure field that can be solved by standard matrix solvers. In our model, the conjugate gradient method with the preconditioner of incomplete Cholesky decomposition is used to solve the resulting sparse and symmetric system of equations.

3.4   Volume of Fluid Method

As explained at the beginning of this section, the volume of fluid method is a means to identify different types of computational cells and thus can be used to track the free surface motion. Letting $\rho(x, y, t) = F(x, y, t)\rho_f$ and substituting this definition and equation (39) into equation (41), we obtain the transport equation for $F(x, y, t)$,

$$\frac{\partial F}{\partial t} + \frac{\partial}{\partial x}(uF) + \frac{\partial}{\partial y}(vF) = 0 \tag{72}$$

For a computational cell centered at (i, j) the above equation can be rewritten in the following finite-difference form

$$F_{i,j}^{n+1} = F_{i,j}^n - \frac{\Delta t}{\Delta x_i}\left(u_{i+\frac{1}{2},j}^{n+1}F_R^n - u_{i-\frac{1}{2},j}^{n+1}F_L^n\right)$$
$$- \frac{\Delta t}{\Delta y_j}\left(v_{i,j+\frac{1}{2}}^{n+1}F_T^n - v_{i,j-\frac{1}{2}}^{n+1}F_B^n\right) \tag{73}$$

in which F_R^n, F_L^n, F_T^n and F_B^n denote the F values on the right, left, top and bottom faces of the computational cell, respectively. Assigning the proper F values on each face of the cell requires some information of the free surface configuration. For instance, the F values in the computational cells centered at (i, j) as shown in figure 3a and 3b are the same. However, the free surface configurations are quite different. Even if the velocities on the right face of the computational cells are the same, one would expect that more fluids are convected across the face in case (b) than in case (a) for small Δt. For this reason a simple free surface reconstruction scheme is needed. In this report, we summarize the Hirt-Nichols algorithm in which the free surface is reconstructed either horizontally or vertically in each free-surface cell based on the F values at the n-th time step. For the cases shown in figure 3, the reconstructed free surface profiles are quite different. The general rule is as follows

$$\left|\frac{\partial F}{\partial y}\right| > \left|\frac{\partial F}{\partial x}\right| \quad \text{and} \quad \frac{\partial F}{\partial x} < 0 \quad \Rightarrow \text{vertical free surface on left side}$$

$$\left|\frac{\partial F}{\partial x}\right| > \left|\frac{\partial F}{\partial y}\right| \quad \text{and} \quad \frac{\partial F}{\partial x} > 0 \quad \Rightarrow \text{vertical free surface on right side}$$

$$\left|\frac{\partial F}{\partial x}\right| < \left|\frac{\partial F}{\partial y}\right| \quad \text{and} \quad \frac{\partial F}{\partial y} < 0 \quad \Rightarrow \text{horizontal free surface on bottom side}$$

$$\left|\frac{\partial F}{\partial x}\right| < \left|\frac{\partial F}{\partial y}\right| \quad \text{and} \quad \frac{\partial F}{\partial y} > 0 \quad \Rightarrow \text{horizontal free surface on top side}$$
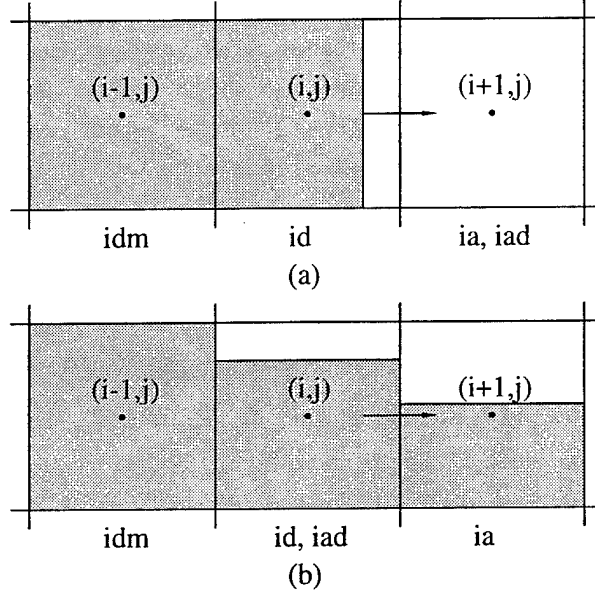
Figure 3: Two types of free surface reconstruction in VOF

The first derivatives of F can be evaluated by using the central difference scheme. For instance

$$
\begin{aligned}
\left(\frac{\partial F}{\partial x}\right)_{i,j}^n &= \frac{\left(\frac{\partial F}{\partial x}\right)_{i+\frac{1}{2},j}^n \Delta x_{i-\frac{1}{2}} + \left(\frac{\partial F}{\partial x}\right)_{i-\frac{1}{2},j}^n \Delta x_{i+\frac{1}{2}}}{\Delta x_{i-\frac{1}{2}} + \Delta x_{i+\frac{1}{2}}} \\
&= \frac{\left[\frac{\Delta x_{i-\frac{1}{2}}}{\Delta x_{i+\frac{1}{2}}}\left(\hat{F}_{i+1,j}^n - \hat{F}_{i,j}^n\right) + \frac{\Delta x_{i+\frac{1}{2}}}{\Delta x_{i-\frac{1}{2}}}\left(\hat{F}_{i,j}^n - \hat{F}_{i-1,j}^n\right)\right]}{\Delta x_{i-\frac{1}{2}} + \Delta x_{i+\frac{1}{2}}}
\end{aligned}
\tag{74}
$$

in which $\hat{F}_{i+1,j}^n$ is the average value of F at the cell $(i+1,j)$ using three vertical neighboring cells, i.e.,

$$
\hat{F}_{i+1,j}^n = \frac{F_{i+1,j+1}^n \Delta y_{j+1} + F_{i+1,j}^n \Delta y_j + F_{i+1,j-1}^n \Delta y_{j-1}}{\Delta y_{j-1} + \Delta y_j + \Delta y_{j+1}}
\tag{75}
$$

Similar formulas can be obtained for $\hat{F}_{i,j}^n$ and $\hat{F}_{i-1,j}^n$.

Once the free surface orientation is determined, the donor-acceptor method is used to advect the F function. For simplicity only the flux in the x-direction will

25

be discussed. Moreover, the x-component of the new velocity on the right face of the computational cell (i,j) is assumed to be positive, i.e., $u_{i+\frac{1}{2},j}^{n+1} > 0$. In the donor-acceptor method, the cell (i,j) is called the donor cell, while the cell $(i+1,j)$ is called the acceptor cell. If $u_{i+\frac{1}{2},j}^{n+1} < 0$, the role of the donor and acceptor cell is switched.

When the free surface configuration in the donor cell is determined to be a horizontal surface, the value for F on the right face is assigned to be the same as that in the donor cell, i.e.

$$F_R^n = F_{i,j}^n = F_{id}^n \tag{76}$$

On the other hand if the free surface configuration in the donor cell is a vertical surface, the F_R value should be more strongly influenced by the F value in the acceptor cell, i.e.

$$F_R^n = F_{i+1,j}^n = F_{ia}^n \tag{77}$$

However, this acceptor method may create the so-called over-filling problem in some situations. Consider the simple one-dimensional case as shown in case (a) of figure 3. The F values in three adjacent cells are $F_{i-1,j}^n = 1.0, F_{i,j}^n = 0.8$ and $F_{i+1,j}^n = 0$. In other words, there is a sharp front in the (i,j) cell. If the acceptor method is used, equation (77) indicates that $F_R^n = 0$.

From the one-dimensional version of (73), one finds that

$$F_{i,j}^{n+1} = F_{i,j}^n + \frac{\Delta t}{\Delta x} u_{i-\frac{1}{2},j}^{n+1} F_L^n$$

in which $F_{i,j}^n = 0.8$ and $F_L^n = 1.0$. Therefore, if the Courant number $Cr = u_{i-1,j}^{n+1} \Delta t / \Delta x$ is greater than 0.2, the F value at the $(n+1)$ time step will be greater than one. To overcome this "over-filling" problem, a corrector term is introduced in the acceptor method, i.e.

$$F_R^n = F_{ia}^n + \Delta F^n \tag{78}$$

where

$$\Delta F^n = max \left\{ \left[\left(F_{dm}^n - F_{ia}^n \right) - \frac{\Delta x_{id}}{u_{i+\frac{1}{2},j}^{n+1} \Delta t} \left(F_{dm}^n - F_{id}^n \right) \right], 0 \right\} \tag{79}$$

and

$$F_{dm}^n = max\left\{F_{id}^n, F_{idm}^n, K\right\} \qquad (80)$$

in which F_{idm}^n denotes the value of F at the cell upstream of the donor cell, which is equal to $id-1$ when $u_{i+\frac{1}{2},j}^{n+1} > 0$. K is a factor used to prevent spurious advection of a small amount of fluid and is often set to be 0.1.

3.5 The $k - \epsilon$ equations

The same nonuniform finite-difference mesh is used to discretize the $k-\epsilon$ equations, (42) and (43). Both k and ϵ are defined at the center of a computational cell. Symbolically, the $k - \epsilon$ equations in the finite-difference form can be written as (Lemos, 1992):

$$\frac{k_{i,j}^{n+1} - k_{i,j}^n}{\Delta t} + FkX - FkY = VISk + \frac{1}{2}\left(P_{i,j}^{n+1} + P_{i,j}^n - \epsilon_{i,j}^{n+1} - \epsilon_{i,j}^n\right) \qquad (81)$$

$$\frac{\epsilon_{i,j}^{n+1} - \epsilon_{i,j}^n}{\Delta t} + F\epsilon X + F\epsilon Y = VIS\epsilon + C_{1\epsilon}\frac{\epsilon_{i,j}^n}{k_{ij}^n}P_{i,j}^{n+1} - C_{2\epsilon}\frac{\epsilon_{i,j}^n}{k_{i,j}^n}\epsilon_{i,j}^{n+1} \qquad (82)$$

In (81) and (82) the advection terms (FkX, FkY, $F\epsilon X$ and $F\epsilon Y$), viscous diffusion terms ($VISk$ and $VIS\epsilon$), and the production terms $P_{i,j}$ need to be defined and described in space. Since the expressions of these terms for the k equation are very similar to those for the ϵ equation, only the details for the k equation are given here.

First, we examine the advection terms. The x-component of the advection term can be written as

$$FkX = \left(u\frac{\partial k}{\partial x}\right)_{i,j} = u_{i,j}^{n+1}\left(\frac{\partial k}{\partial x}\right)_{i,j}^n \qquad (83)$$

Note that the derivative of k is evaluated at the n-th time level, which makes the scheme explicit. The finite difference form of the spatial derivative for k, $\partial k/\partial x$, is the same as that for $\partial u/\partial x$. Thus

$$\left(\frac{\partial k}{\partial x}\right)_{i,j}^n = \left\{\left[1 + \gamma\, sgn\left(u_{i,j}^{n+1}\right)\right]\Delta x_{i+\frac{1}{2}}\left(\frac{\partial k}{\partial x}\right)_{i-\frac{1}{2}}^n\right.$$
$$\left. + \left[1 - \gamma\, sgn\left(u_{i,j}^{n+1}\right)\right]\Delta x_{i-\frac{1}{2}}\left(\frac{\partial k}{\partial x}\right)_{i+\frac{1}{2},j}^n\right\} /$$
$$\left[\Delta x_{i+\frac{1}{2}} + \Delta x_{i-\frac{1}{2}} + \gamma\left(\Delta x_{i+\frac{1}{2}} - \Delta x_{i-\frac{1}{2}}\right)\right] \qquad (84)$$

where

$$\left(\frac{\partial k}{\partial x}\right)^{n}_{i-\frac{1}{2},j} = \frac{k^{n}_{i,j} - k^{n}_{i-1,j}}{\Delta x_{i-\frac{1}{2}}} \qquad (85)$$

$$\left(\frac{\partial k}{\partial x}\right)^{n}_{i+\frac{1}{2},j} = \frac{k^{n}_{i+1,j} - k^{n}_{i,j}}{\Delta x_{i+\frac{1}{2}}} \qquad (86)$$

and γ is the coefficient weighting the relative importance between the central difference and the upwind scheme, similar to α in the finite difference form of momentum advection. In the actual computation, γ is generally chosen to be the unity that makes the advection terms discretized by the upwind scheme. Such scheme ensures the stable solution for the k equation under any circumstance. However, it is found that for most computations, as long as γ is greater than 0.5, almost the same stable solutions will be obtained.

The y-component of the advection term can be expressed in the similar form as (83)

$$FkY = \left(v\frac{\partial k}{\partial y}\right)_{i,j} = v^{n+1}_{i,j}\left(\frac{\partial k}{\partial y}\right)^{n}_{i,j} \qquad (87)$$

and

$$\left(\frac{\partial k}{\partial y}\right)^{n}_{i,j} = \left\{\left[1 + \gamma\,sgn\left(v^{n+1}_{i,j}\right)\right]\Delta y_{j+\frac{1}{2}}\left(\frac{\partial k}{\partial x}\right)^{n}_{i,j-\frac{1}{2}}\right.$$
$$\left. + \left[1 - \gamma\,sgn\left(v^{n+1}_{i,j}\right)\right]\Delta y_{j-\frac{1}{2}}\left(\frac{\partial k}{\partial y}\right)^{n}_{i,j+\frac{1}{2}}\right\}$$
$$/\left[\Delta y_{j+\frac{1}{2}} + \Delta y_{j-\frac{1}{2}} + \gamma\left(\Delta y_{j+\frac{1}{2}} - \Delta y_{j-\frac{1}{2}}\right)\right] \qquad (88)$$

in which

$$\left(\frac{\partial k}{\partial y}\right)^{n}_{i,j-\frac{1}{2}} = \frac{k^{n}_{i,j} - k^{n}_{i,j-1}}{\Delta y_{j-\frac{1}{2}}} \qquad (89)$$

$$\left(\frac{\partial k}{\partial y}\right)^{n}_{i,j+\frac{1}{2}} = \frac{k^{n}_{i,j+1} - k^{n}_{i,j}}{\Delta y_{j+\frac{1}{2}}} \qquad (90)$$

The viscous term in (81) is defined as:

28

$$VISk = \left\{ \frac{\partial}{\partial x} \left[(\frac{\nu_t}{\sigma_k} + \nu) \frac{\partial k}{\partial x} \right] + \frac{\partial}{\partial y} \left[(\frac{\nu_t}{\sigma_k} + \nu) \frac{\partial k}{\partial y} \right] \right\}^n_{i,j} \qquad (91)$$

The first term in above equation can be discretized with the central difference method,

$$\left\{ \frac{\partial}{\partial x} \left[\left(\frac{\nu_t}{\sigma_k} + \nu\right) \frac{\partial k}{\partial x} \right] \right\}^n_{i,j} = \frac{\left(\frac{\nu_t}{\sigma_k} + \nu\right)^n_{i+\frac{1}{2},j} \left(\frac{\partial k}{\partial x}\right)^n_{i+\frac{1}{2},j} - \left(\frac{\nu_t}{\sigma_k} + \nu\right)^n_{i-\frac{1}{2},j} \left(\frac{\partial k}{\partial x}\right)^n_{i-\frac{1}{2},j}}{\Delta x_i}$$

$$= \frac{1}{\Delta x_i} \left[\left(\frac{\nu_t}{\sigma_k} + \nu\right)^n_{i+\frac{1}{2},j} \frac{k^n_{i+1,j} - k^n_{i,j}}{\Delta x_{i+\frac{1}{2}}} - \left(\frac{\nu_t}{\sigma_k} + \nu\right)^n_{i-\frac{1}{2},j} \frac{k^n_{i,j} - k^n_{i-1,j}}{\Delta x_{i-\frac{1}{2}}} \right] \qquad (92)$$

and the second term can be similarly obtained,

$$\left\{ \frac{\partial}{\partial y} \left[\left(\frac{\nu_t}{\sigma_k} + \nu\right) \frac{\partial k}{\partial y} \right] \right\}^n_{i,j} = \frac{\left(\frac{\nu_t}{\sigma_k} + \nu\right)^n_{i,j+\frac{1}{2}} \left(\frac{\partial k}{\partial y}\right)^n_{i,j+\frac{1}{2}} - \left(\frac{\nu_t}{\sigma_k} + \nu\right)^n_{i,j-\frac{1}{2}} \left(\frac{\partial k}{\partial y}\right)^n_{i,j-\frac{1}{2}}}{\Delta y_j}$$

$$= \frac{1}{\Delta y_j} \left[\left(\frac{\nu_t}{\sigma_k} + \nu\right)^n_{i,j+\frac{1}{2}} \frac{k^n_{i,j+1} - k^n_{i,j}}{\Delta y_{j+\frac{1}{2}}} - \left(\frac{\nu_t}{\sigma_k} + \nu\right)^n_{i,j-\frac{1}{2}} \frac{k^n_{i,j} - k^n_{i,j-1}}{\Delta y_{j-\frac{1}{2}}} \right] \qquad (93)$$

where the value of $\left(\frac{\nu_t}{\sigma_k} + \nu\right)^n$ defined at the cell face can be obtained with linear interpolation, i.e.,

$$\left(\frac{\nu_t}{\sigma_k} + \nu\right)^n_{i+\frac{1}{2},j} = \frac{\Delta x_i (\frac{\nu_t}{\sigma_k} + \nu)^n_{i+1,j} + \Delta x_{i+1} (\frac{\nu_t}{\sigma_k} + \nu)^n_{i,j}}{\Delta x_i + \Delta x_{i+1}} \qquad (94)$$

The production term $P_{i,j}$ is evaluated at both the n-th and $(n + 1)$-th time steps. At the n-th time step, we have:

$$P^n_{i,j} = \nu_t \left[2 \left(\frac{\partial u}{\partial x}\right)^2_{i,j} + 2 \left(\frac{\partial v}{\partial y}\right)^2_{i,j} + \left(\frac{\partial u}{\partial y} + \frac{\partial v}{\partial x}\right)^2_{i,j} \right]^n \qquad (95)$$

with the following finite difference forms:

$$\left(\frac{\partial u}{\partial x}\right)^n_{i,j} = \frac{u^n_{i+\frac{1}{2},j} - u^n_{i-\frac{1}{2},j}}{\Delta x_i} \qquad (96)$$

$$\left(\frac{\partial v}{\partial y}\right)_{i,j}^{n} = \frac{v_{i,j+\frac{1}{2}}^{n} - v_{i,j-\frac{1}{2}}^{n}}{\Delta y_j} \tag{97}$$

$$\left(\frac{\partial v}{\partial x}\right)_{i,j}^{n} = \frac{v_{i+\frac{1}{2},j}^{n} - v_{i-\frac{1}{2},j}^{n}}{\Delta x_i} \tag{98}$$

$$\left(\frac{\partial u}{\partial y}\right)_{i,j}^{n} = \frac{u_{i,j+\frac{1}{2}}^{n} - u_{i,j-\frac{1}{2}}^{n}}{\Delta y_j} \tag{99}$$

The value of $P_{i,j}^{n+1}$ can be similarly obtained.

3.6 Stability Analysis for Numerical Model

The governing equations (40) to (43) are essentially the transient advection-diffusion equations. The explicit finite difference form for these equations are subject to the numerical instability unless certain stability criteria are satisfied. Due to the intrinsic nonlinearity in the governing equations, the general stability analysis method, i.e., von Neumann method, is not applicable. In order to overcome this difficulty, we first linearize the governing equations and then perform the standard von Neumann stability analysis to obtain the stability criteria for the linear case:

$$\Delta t \leq min\left\{\frac{u}{\Delta x}, \frac{v}{\Delta y}\right\} \tag{100}$$

$$\Delta t \leq min\left\{\frac{1}{2(\nu + \nu_t)}\left[\frac{(\Delta x)^2(\Delta y)^2}{(\Delta x)^2 + (\Delta y)^2}\right]\right\} \tag{101}$$

The above criteria are obtained by assuming the advection term is discretized by upwind scheme. The first criterion arises from the stability requirement for the advection term and the second from the diffusion term. In practice, due to the effect of nonlinearity and the combination of the central difference method that will further restrict the stability condition, some empirical coefficients that are less than unity are multiplied to the original time step restriction to ensure the practical stability in the computation. These coefficients are $\frac{3}{10}$ for (100) and $\frac{2}{3}$ for (101).

3.7 Computational Cycle

Finally, the complete cycle for updating the field variables for one time step is summarized as follows:

1. Compute the tentative velocities using equation (44).

2. Apply the tentative boundary conditions (tangential stress and divergence free) on the free surface as well as the inflow boundary condition if necessary.

30

3. Update the pressure field according to equation (47), which automatically incorporates the normal stress boundary condition.

4. Obtain the final velocities according to equation (45).

5. Apply again the boundary conditions on the free surface.

6. Update k and ϵ value using new velocities.

7. Update the VOF function.

8. Apply the final boundary condition, mainly to the newly filled. cell that was originally empty in the previous time step

4 Detailed Numerical Treatments in RIPPLE and Modifications in Present Model

In this section, some detailed numerical treatments in RIPPLE will be discussed. A few modifications have been made to improve the accuracy of the numerical computations. The major modifications appear on the applications of boundary conditions on the free surface. Efforts have also been made to improve the accuracy of numerical solution to the PPE and the momentum conservation equation near the solid boundaries.

4.1 Boundary Conditions on Free Surface

In RIPPLE, the velocity field at the new time step for both the interior cells and surface cells are obtained by using the projection method. Then the divergence free criterion is imposed on the free surface cell to adjust the velocity at the interface between the surface cell and empty cell. For example, for cell (i,j), $u_{i+\frac{1}{2},j}$, $u_{i-\frac{1}{2},j}$, and $v_{i,j-\frac{1}{2}}$ are obtained by the projection method, but $v_{i,j+1}$ is obtained by using the divergence free criterion, $\frac{\partial u}{\partial x} + \frac{\partial v}{\partial y} = 0$, which leads to $v_{i,j+\frac{1}{2}} = v_{i,j-\frac{1}{2}} - \frac{\Delta y}{\Delta x}(u_{i+\frac{1}{2},j} - u_{i-\frac{1}{2},j})$ (Figure 4).

In RIPPLE, there is no explicit dynamic boundary conditions applied on the free surface. The only criterion enforced on the free surface is divergence free that ensures the mass conservation on the free surface. It is found that this approach will create large spurious velocity on the free surface that significantly affects the accuracy of velocity and vorticity computation nearby. The modifications are made in the following aspects:
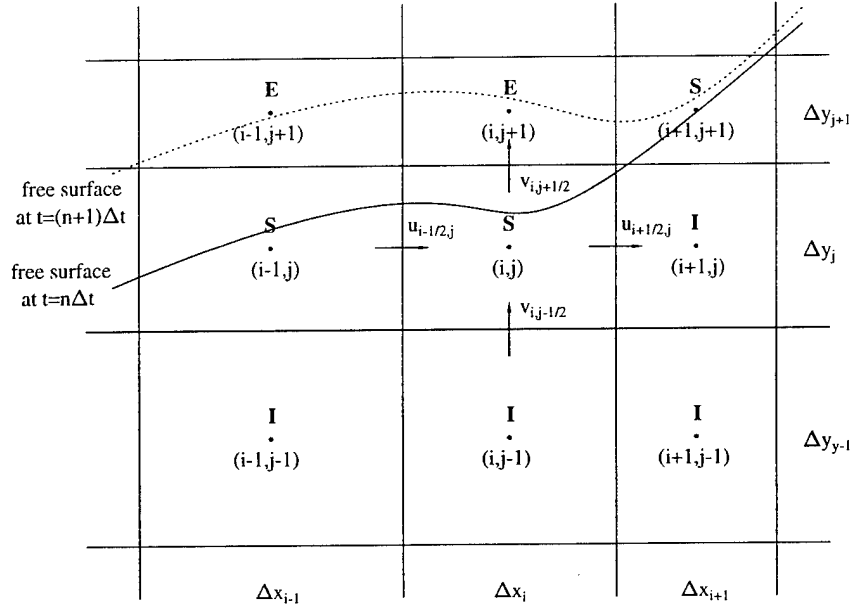
Figure 4: Boundary conditions and new-filled cell treatment on free surface

4.1.1 Tangential Stress Boundary Conditions

In our computations, the air effect is neglected so that the tangential stress boundary condition becomes: $\frac{\partial u_n}{\partial x_t} + \frac{\partial u_t}{\partial x_n} = 0$. For nearly horizontal free surface, the above equation becomes: $\frac{\partial u}{\partial y} + \frac{\partial v}{\partial x} = 0$. For the cell $(i-1, j)$, conventionally the boundary condition is applied at point $(i - \frac{1}{2}, j + \frac{1}{2})$ (Lemos, 1992). Thus, the corresponding finite difference form becomes: $\frac{u_{i-\frac{1}{2},j+1} - u_{i-\frac{1}{2},j}}{\Delta y_{j+\frac{1}{2}}} + \frac{v_{i,j+\frac{1}{2}} - v_{i-1,j+\frac{1}{2}}}{\Delta x_{i-\frac{1}{2}}} = 0$ (Figure 4). The outside fictional tangential velocity $u_{i-1/2,j+1}$ can be found from the above expression provided that the other three quantities are known. We have found that this treatment can still generate large errors in the velocity computations on the free surface. The errors in the velocity computation are mainly due to the fact that the pressure computed on the free surface usually contains large errors. The errors in the pressure computation on free surface cell arise from the fact that in RIPPLE the normal stress cannot be applied onto the exact free surface in general when the PPE is solved. Fortunately, the pressure computed just one cell away from the free surface is very accurate. This phenomenon is caused by the particular method in RIPPLE to solve the PPE and will be discussed later in detail.

Realizing that the pressure computed on the free surface may contain large errors, which in turn affects the tangential velocity computations, we decide to apply the tangential stress boundary condition one cell down from the free surface. For instance, for cell $(i-1, j)$, instead of applying the boundary condition at the point $(i - \frac{1}{2}, j + \frac{1}{2})$, we apply the boundary condition at the point $(i - \frac{1}{2}, j - \frac{1}{2})$ and obtain

32

$u_{i-\frac{1}{2},j}$ by using $u_{i-\frac{1}{2},j-1}$, $v_{i,j-\frac{1}{2}}$, and $v_{i-1,j-\frac{1}{2}}$. By so doing, we obtain the velocities between surface cells not by using the projection method, but by employing the tangential stress boundary condition. Because the computed pressure of the cell beneath the free surface is very accurate, the new way for obtaining the velocity on the free surface is much more accurate than the conventional method.

4.1.2 Newly Filled Cell Treatment

After updating the VOF function, the new surface cells may be created, which were originally empty at the previous time step. RIPPLE fails to apply the correct boundary condition for this situation. Chen et al. (1995) addressed this problem and proposed the momentum-capturing method to define the velocity for those newly filled cells. The basic idea for their method is to assume the newly filled cell carries the momentum of its neighborhood. For example, in figure 4, cell $(i-1,j+1)$ is empty at the end of n-th time step but is partially filled at the end of $(n+1)$-th time step. In RIPPLE, $u_{i-\frac{1}{2},j+1} = 0$ at the end of $(n+1)$-th time step. This will affect the accuracy of velocity computations near the free surface at $(n+2)$-th time step. On the other hand, Chen et al. (1995) assigned $u_{i-\frac{1}{2},j+1} = u_{i-\frac{1}{2},j}$ at the end of $(n+1)$-th time step that ensures the accuracy of the velocity computation on the free surface. Our model follows the same idea as Chen et al.'s to define the velocity at the newly filled cells.

4.2 PPE Computation

During the computation of PPE, the normal stress boundary condition is naturally incorporated. In most of situations, the air effect and the normal stress due to the fluid on the free surface is neglected, which simplifies the normal stress condition to be $p = 0$ on the free surface from equation (4). Since the free surface seldom passes the cell center where the pressure is defined, the application of the normal stress boundary condition on the free surface becomes a challenging task. In the MAC method, the accuracy of applying normal stress boundary condition can be improved by using the irregular star method (Chan and Street, 1970) and the micro cells treatment (Raad et al., 1994). These methods, however, cannot be readily extended to the VOF method where the free surface location is not exactly defined.

Realizing this limitation, RIPPLE uses another approach to treat the normal stress boundary condition. Instead of attempting to apply the pressure on the exact location of the free surface, the approximation is made to assume the free surface cell is the cell with variable density fluid in which the density at the cell center is represented by the VOF function, $\rho_c = \rho_f F$ (Figure 5). Such an approximation is consistent with the approximation we made before in equations (6), (13), and (41) that the free surface has a finite thickness filled by stratified fluids. Thus, the free surface is always assumed to be located at the center of empty cell just

above the free surface cell during the PPE computation. The above approximation, though crude, is simple to use and provides the very accurate pressure solution one cell away from the free surface cell. The disadvantage of the method is that the pressure computed right in the surface cell may contain large errors. These errors may contaminate the tangential velocities computation on the free surface.
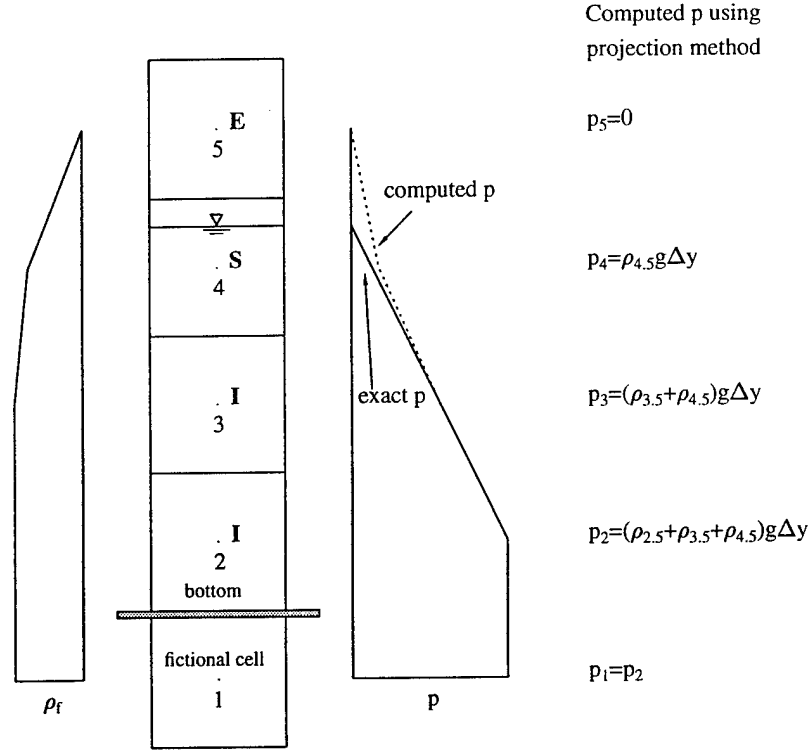

Figure 5: An example of PPE computations for one-dimensional problem

To understand why the pressure computed on the free surface may contain large errors and the pressure one cell below is almost exactly computed, we will examine the following simple example. The one-dimensional case with the still water free surface above the fourth cell center (Figure 5) will be examined. The constant grid size Δy will be used in the numerical computation. Assuming initially there is no flow motion, we expect that the fluid will remain still and the pressure distribution should be hydrostatic. Numerically, we hope that by advancing one time step from initially still condition, the fluid can stay still and the pressure hydrostatic. Following the standard project method described before, we will first find out that the tentative velocity without using the pressure information. Then we solve the PPE with known tentatively velocity divergence. By imposing the boundary condition on the free surface $p_5 = 0$ and on the solid bottom $p_1 = p_2$, it is very easy to find the solution to the PPE to be: $p_4 = \rho_{4\frac{1}{2}} g \Delta y$, $p_3 = (\rho_{4\frac{1}{2}} + \rho_{3\frac{1}{2}}) g \Delta y$, and $p_2 = (\rho_{4\frac{1}{2}} + \rho_{3\frac{1}{2}} + \rho_{2\frac{1}{2}}) g \Delta y$. Now, let's inspect the pressure in the cell right beneath the free surface, cell 3. Since ρ is represented by the VOF function $\rho = F \rho_f$ and

34

the value of F at the cell face can be obtained by linear interpolation of F in the cell center, we may rewrite $p_3 = \rho_f g[(F_4 + \frac{1}{2}F_3)\Delta y]$. It is ready to show that the pressure computed there is exactly hydrostatic and so are all cells beneath. The pressure on the free surface is found to be $p_4 = \frac{1}{2}F_4\rho_f g\Delta y$. It is ready to observe that the pressure computed on the free surface cell may deviate from the true pressure and thus can affect the final tangential velocity computation for the two-dimensional problem. One effective way to reduce the influence of pressure errors is to adapt the new method to apply the tangential stress boundary condition on the free surface as introduced in the previous section.

During the testing of RIPPLE, another error is found in RIPPLE which reduces the accuracy of solution to the PPE when a variable mesh size is used. Referring back to equation (70a), when the spatial derivative of p at the cell face, for example, $\left(\frac{\partial p}{\partial x}\right)_{i+\frac{1}{2}}^{n+1}$, is discretized, we will have $\frac{p_{i+1}^n - p_i^n}{\Delta x_{i+\frac{1}{2}}}$. Instead of using $x_{i+\frac{1}{2}} = \frac{1}{2}(\Delta x_i + \Delta x_{i+1})$, which represents a first order accurate discretization for the variable grid, RIPPLE uses $\frac{1}{\Delta x_{i+\frac{1}{2}}} = \frac{1}{2}(\frac{1}{\Delta x_i} + \frac{1}{\Delta x_{i+1}})$, which is only zeroth order accurate.

4.2.1 Partial Cell Treatment

Partial cell treatment is a special tool used in RIPPLE to handle the unstructured interior obstacle and solid boundary. As introduced at the beginning of previous section, the basic idea behind this technique is that the obstacle can be modeled as a special case of two-phase flow with infinite density. Compared with the conventional way to treat irregular solid wall that creates the saw-tooth shape of boundary, partial cell treatment partially block the cell face and cell itself according to the real geometry of the boundary. With the use of the partial cell treatment, the variables in cells or cell faces are redefined as the multiplication of openness coefficients with original variables, representing the mean values there. Near the obstacle, the openness coefficients are less than unit that makes the mean quantities smaller than their original values. The governing equations for the general turbulent flow can be rewritten as:

$$\frac{\partial(\theta u_i)}{\partial x_i} = 0 \qquad (102)$$

$$\frac{\partial(\theta u_i)}{\partial t} + \theta u_j \frac{\partial(\theta u_i)}{\partial x_j} = -\frac{\theta}{\rho}\frac{\partial p}{\partial x_i} + \theta g_i + \theta\frac{\partial}{\partial x_j}[2(\nu_t + \nu)\sigma_{ij}] - \frac{2\theta}{3}\frac{\partial k}{\partial x_i} \qquad (103)$$

In RIPPLE, the advection terms is written as $\frac{\partial(\theta u_i u_j)}{\partial x_j}$ for the conservative scheme with one θ missing. It is found that RIPPLE's approach sometimes causes instability during the runup when θ is small in some location where u_i is relatively large, while equation (103) eliminates such numerical instability.

5 Numerical Examples

In this section, we will verify our model by performing the numerical experiments for a series of testing problems. These testing problems are in the order of increasing complexity. The first group of the numerical experiments is for laminar flow without turbulence. The purpose of such testing is to demonstrate the capability of the solver to the NSE. Without losing generality, we use three examples for numerical testing. One is the motion of initially tilting fluid in a rectangular tank. The numerical results are compared to the linear wave solution. The second example is the solitary wave propagation on the constant water depth. The numerical results of the wave profiles are compared to the analytical solutions based on the Boussinesq equation. The third example is the nonbreaking solitary wave runup on a uniform slope. The numerical results are compared to the BIEM results based on potential flow theory and experimental measurements. This test shows the capability of the partial cell treatment in handling the unstructured bottom topography. The second group of the numerical experiments are for turbulence flows. The purpose of such testing is to validate the turbulence model used in the computation. The validation of the turbulence model is generally very difficult. For a well-developed turbulent flow without free surface, the $k - \epsilon$ model has been sufficiently verified in the previous studies as summarized by Rodi (1980). The verification of the $k - \epsilon$ model for a transient flow with free surface, however, is rarely conducted before. The example we choose is the breaking solitary wave runup on beach (Synolakis, 1986; Zelt, 1991). The simulated wave profiles will be compared with experimental measurements.

5.1 Laminar Oscillating Fluids in a Tank

In this example, flow oscillations in a rectangular tank are simulated. The free surface of the fluid in the tank is initially at an inclined position (Figure 6(a)). After the initial moment, the fluid begins to move under gravity. Since the flow motions are restricted in the tank on both sides, the motions can be decomposed into infinite modes of standing waves with the maximum wave length of $L = 2W$, where W is the width of the tank. Mathematically, the free surface displacement $\eta(x,t)$ can be written as:

$$\eta(x,t) = \sum_{n=1}^{\infty} a_n \sin(k_n x) \cos(\omega_n t) \qquad (104)$$

where $k_n = \frac{2n\pi}{L}$ is the wave number of the n-th mode, ω_n the frequency of the n-th mode and can be determined by the dispersion relationship, $\omega_n = \sqrt{gk_n \tanh(k_n d)}$, with d being the still water depth. a_n, the wave amplitude of the n-th mode, can be determined by using the initial condition,

$$a_n = \frac{sL}{2n^2\pi^2}\left[4\sin(\frac{n\pi}{2}) - 2\sin(n\pi)\right] \tag{105}$$

where s is the slope of the initially inclined free surface. The analytical solution is accurate as long as the linear wave theory is valid. In the actual computations of the analytical solution, 40 modes are used which are sufficient to resolve the the free surface variations. In the numerical computations, the width of the tank $W = 0.2m$, the water depth $d = 0.04m$, and the initial free surface slope $s = 0.1$. Total 40×80 meshes (non-uniform in vertical direction) are placed onto the computational domain. The time step Δt is adjusted automatically during the computation so that $Cr = max(\frac{u\Delta t}{\Delta x}, \frac{v\Delta t}{\Delta y}) = 0.3$. This guarantees the practical stability while at the same time maintains the computational efficiency. The molecular viscosity is neglected in the computation to simulate the potential flow. It has been shown that such simplification has a negligible effect to the numerical results.

Figures 6(a) to 6(l) give the comparison of the analytical solution (104) and (105) to the numerical results. The comparisons show that the numerical results agree very well with the analytical solution after about one period for the slowest mode, $T_1 = \frac{2\pi}{\omega_1} = 0.507s$. The small discrepancies in the comparisons could be caused by both the linear wave approximation for finite amplitude waves and the numerical truncation errors in the finite difference scheme. The VOF method behaves very well in tracking free surface, even though there are more than one major modes during the motion. Such characteristics of numerical scheme is very useful for the breaking wave simulation, where shorter waves are generated during the breaking process.

It is noted that different grid systems varying from 20×30 to 80×120 have been used to check the sensitivity of numerical results to grid system used. It is found that the numerical results computed with different grid system are fairly close. In the next examples, the similar sensitivity analysis for grid systems has also been performed and the final choice of mesh size is determined by considering both computational efficiency and numerical accuracy.

5.2 Solitary Waves Propagation on Constant Water Depth

The solitary wave propagation on the constant water depth is a classical testing problem for a wave simulation model. The solitary wave is a finite amplitude wave with the permanent shape. The nonlinearity and frequency dispersion are perfectly balanced during the wave propagation. The analytical solution for the wave profile can be derived from the Boussinesq equation (Lee et al., 1982),

$$\eta(x,t) = a\,\text{sech}^2\left[\sqrt{\frac{3a}{4d^3}}\,(x - ct)\right] \tag{106}$$
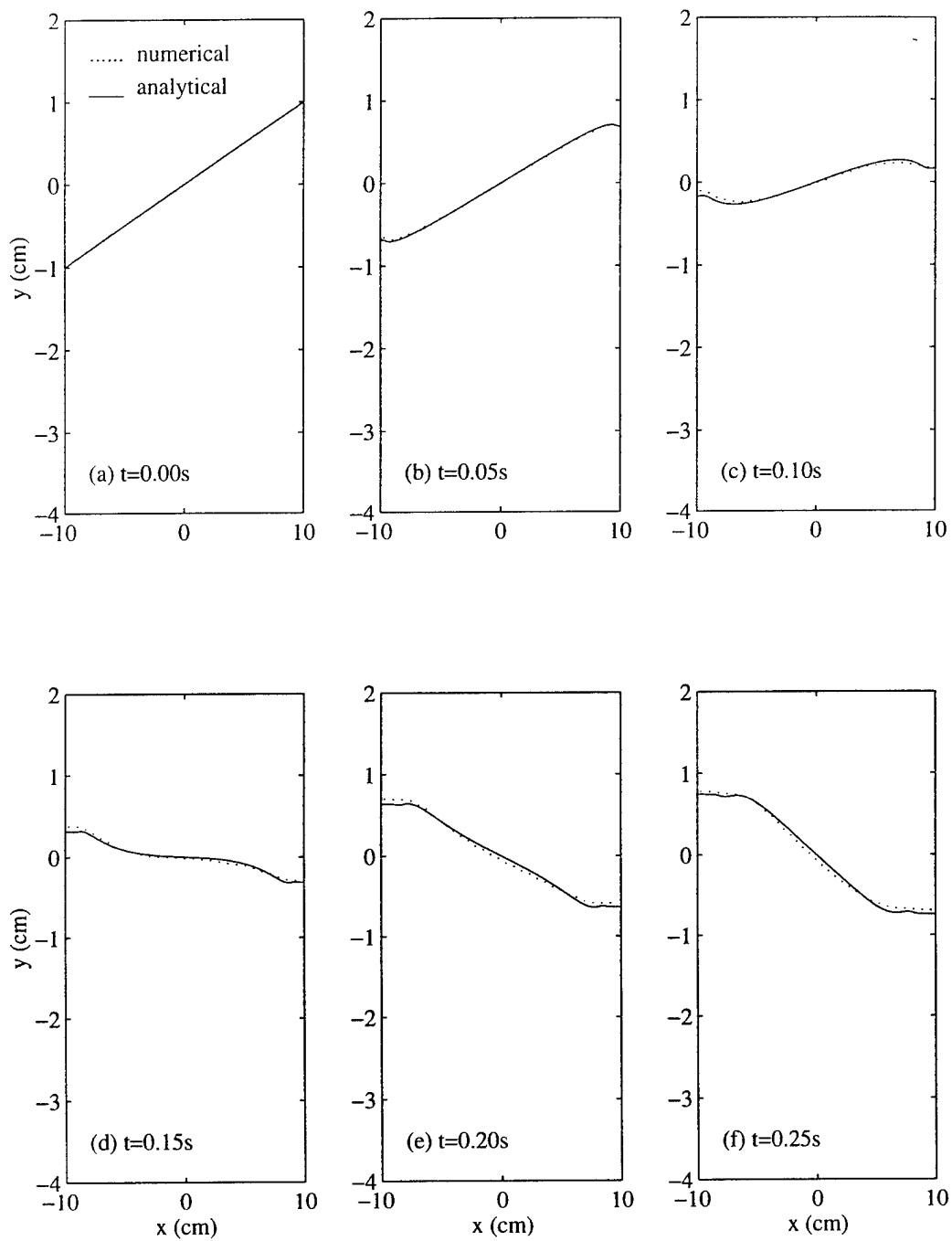
37

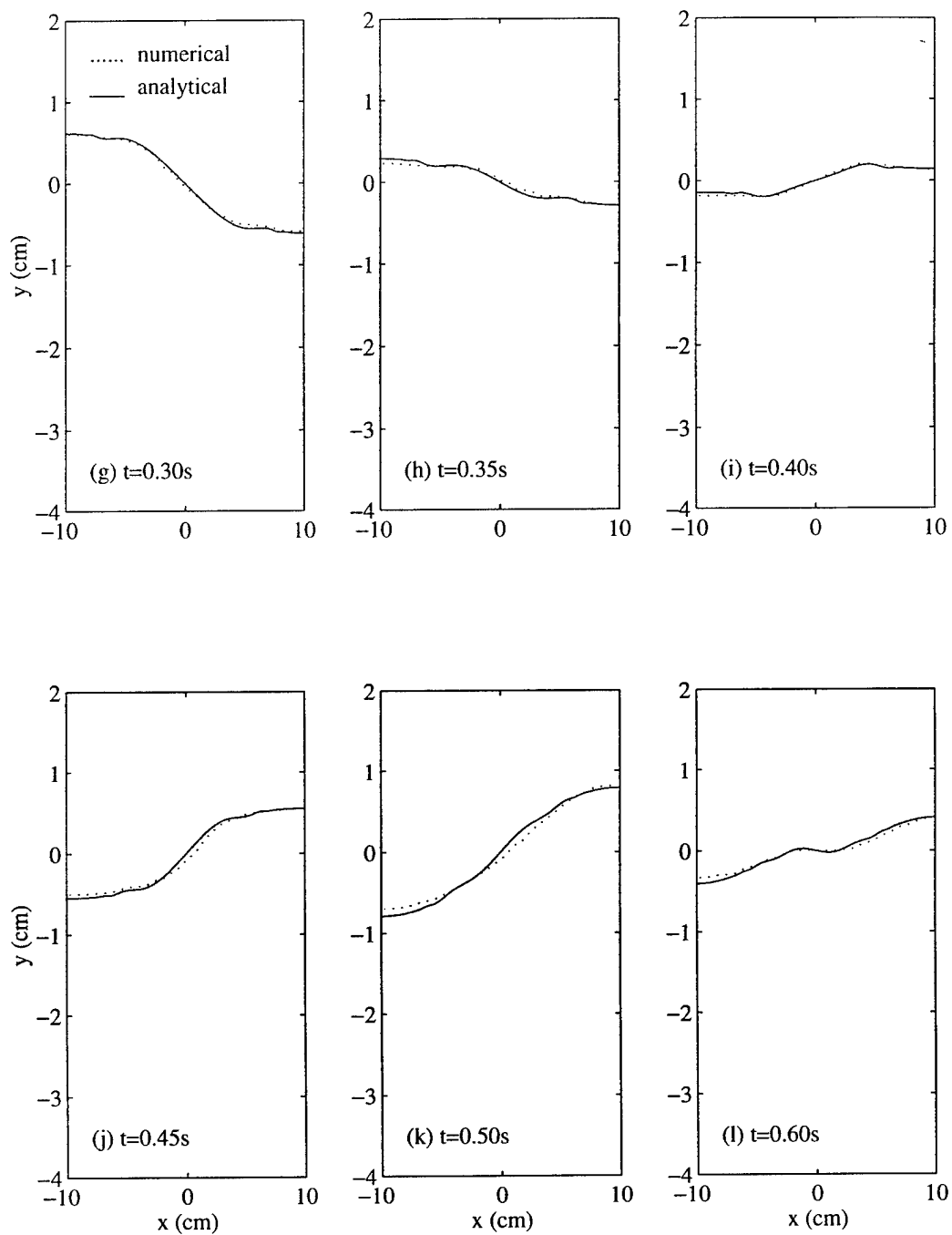Figure 6: Flow ocsillations in a tank

Figure 6: Flow ocsillations in a tank

where a is the wave amplitude and $c = \sqrt{gd(1 + \frac{a}{d})}$ is the wave celerity.

Three cases are investigated in this example, with different ratios of the wave amplitude to the still water depth of $a/d = 0.1$, $a/d = 0.2$, and $a/d = 0.3$ The still water depth is $d = 1m$ for three tests. In the numerical computations, the same discretizations of $\Delta x = 0.1m$ and $\Delta y = 0.01m$ are used for three tests with $0m \leq x \leq 100m$. The time step Δt is automatically adjusted during the computation to satisfy the stability constraints by both the advection and diffusion processes, i.e., equations (100) and (101). The velocity u and v and free surface displacement η are specified at the left boundary based on the Boussinesq analytical solution for a solitary wave (Lee at al, 1982).

Figure 7 shows the comparisons between the simulated wave profiles and the analytical solutions. In Figure 7(a), the case of $a/d = 0.1$ is presented. It is observed that the numerical results agree with the analytical solution perfectly even after the propagation of about $100d$. This test verifies the accuracy of the numerical model under small value of a/d. Figures 7(b) and 7(c) shows the case of $a/d = 0.2$ and $a/d = 0.3$. It is found that the discrepancies between the numerical results and the analytical solutions increase as the increase of a/d, especially after a long distance of propagation. These discrepancies could be caused by two factors. One is that as the increase of a/d, the numerical dissipation increases accordingly because the numerical dissipation rate is proportional to $O(u\Delta x)$, while u is proportional to a/d. On the other hand, as the increase of a/d, the Boussinesq equation, which neglects the higher order nonlinear and dispersive terms, may not be sufficient to approximate the original NSE.

5.3 Nonbreaking Solitary Wave Runup on Beach

In this example, the nonbreaking solitary wave runups on a steep beach with the slope of 30° are investigated. The toe of the beach is $6.49m$ away from the wave maker. The still water depth is $0.16m$ and the wave amplitude is $0.027m$. Numerical computations using BIEM method are performed for the whole domain, from the wave-maker to the shoreline. The number of nodes is 121 on the free surface, 51 along the bottom, 11 on the sloping beach, and 6 on the wave maker. The time step is $\Delta t = 0.01s$. The numerical computations using the VOF method is performed in a smaller domain near the shoreline with $4.49m \leq x \leq 6.99m$ and $-0.16m \leq y \leq 0.11m$. The computational domain is discretized with a 250×90 uniform grid systems with $\Delta x = 0.01m$ and $\Delta y = 0.003m$. The fixed time step $\Delta t = 0.004s$ is used that produces a stable solution. The velocity u and v and free surface displacement η are specified at the left boundary similarly to that in section 5.2. The velocity is measured by a particle image velocimetry (PIV) system (Adrian, 1991). Figure 8 gives the sketch of the computational domain and the measurement section.

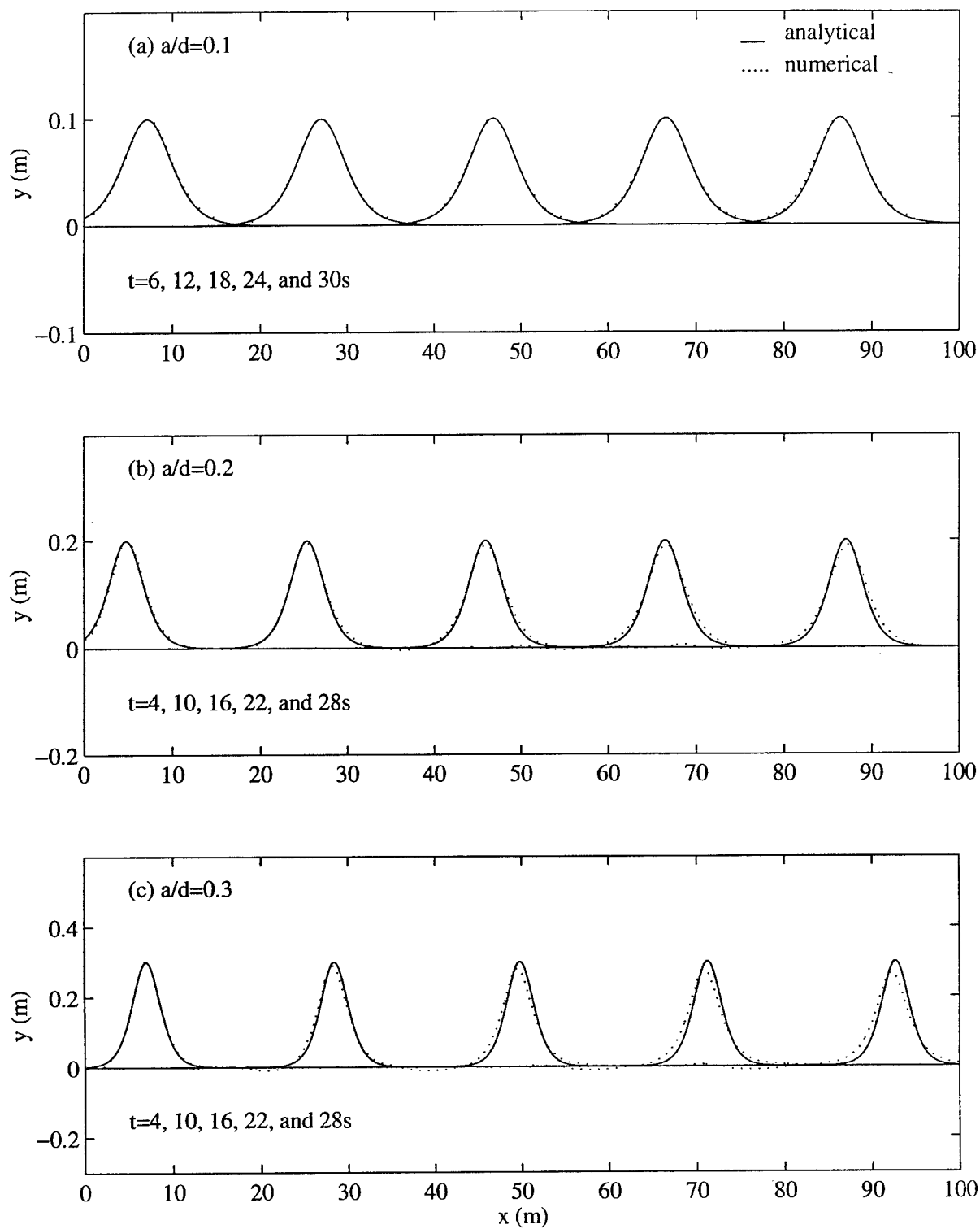The results of the nonbreaking solitary wave are shown in figure 9 which includes

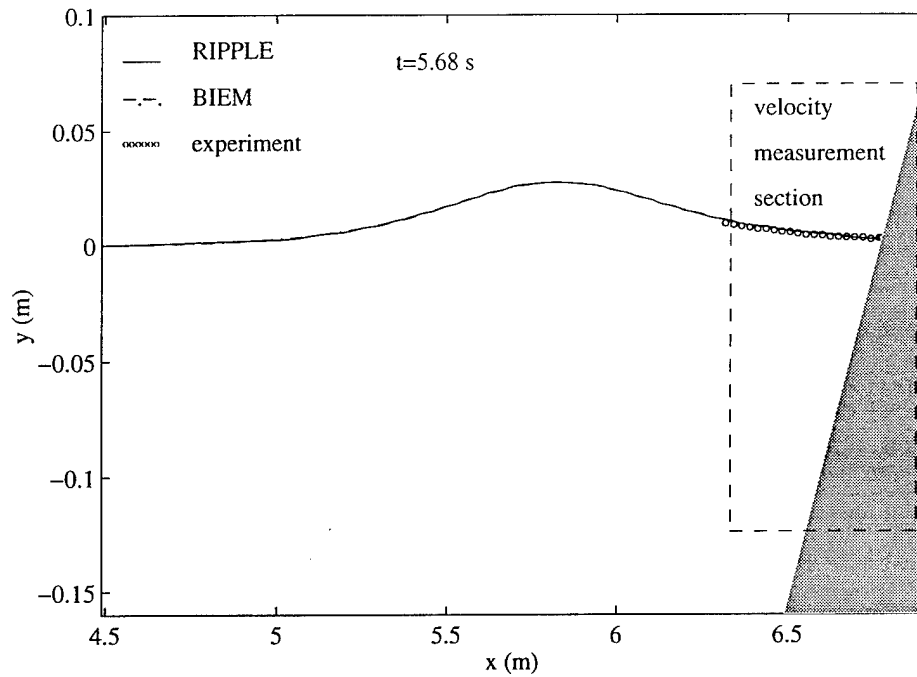Figure 7: Solitary wave propagation on constant water depth

Figure 8: Computational domain for VOF and measurement section for PIV

the VOF, BIEM, and PIV results for the free surface profile and internal velocity. Figure 9(a) to 8f show the time series of solitary wave runup, rundown, and re-runup on the steep beach. The overall agreement of the free surface profiles between the experimental measurements and numerical computations are excellent. The comparisons of the internal velocity at different time are also very good. Some discrepancies are observed between experimental data and numerical results when wave runup reaches its highest point and rundown reaches its lowest point. It is noted that the BIEM results and the VOF method results always agree very well. Since the BIEM results for potential flow are very accurate, they can serve here as the reference for both the experimental measurements by the PIV and the numerical results by the VOF method.

Figure 9(a) shows the snapshot when the wave is climbing up the slope ($t = 6.38s$). It is interesting to observe that the particles in the wave front move in the same direction as the beach slope orientation. The particles at the farthest runup tip possess the maximum velocity. Velocity decreases downward and backward due to the negative pressure by the runup wave. In this frame, experimental data and numerical results agree very well. Figure 9(b) ($t = 6.58s$) shows the velocity distribution when the wave almost reaches its highest runup point. Except for the very small tip that still has the forward and upward velocity, the major portion of fluid on the slope has started the rundown process. In this frame, the comparison
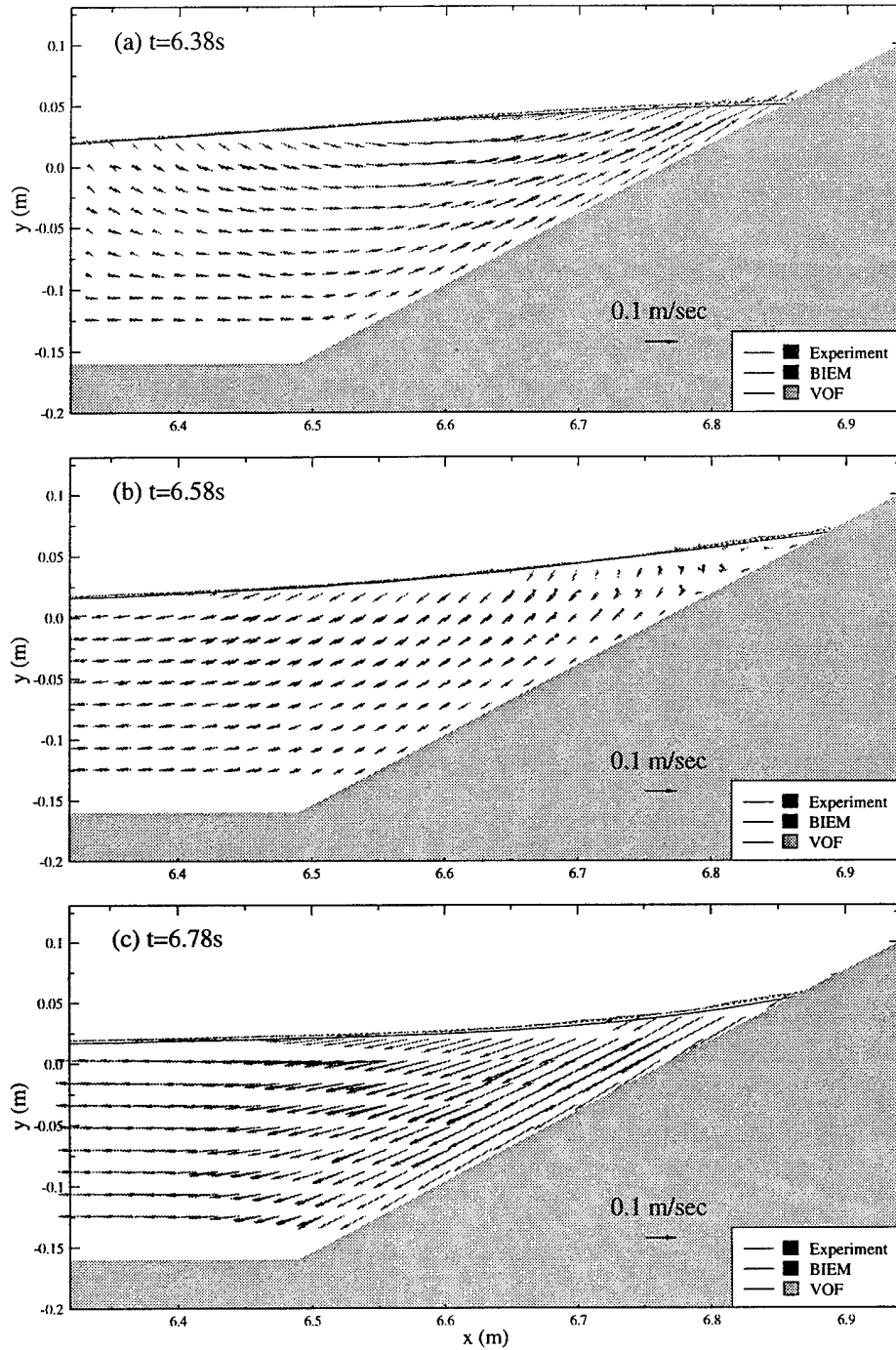
42

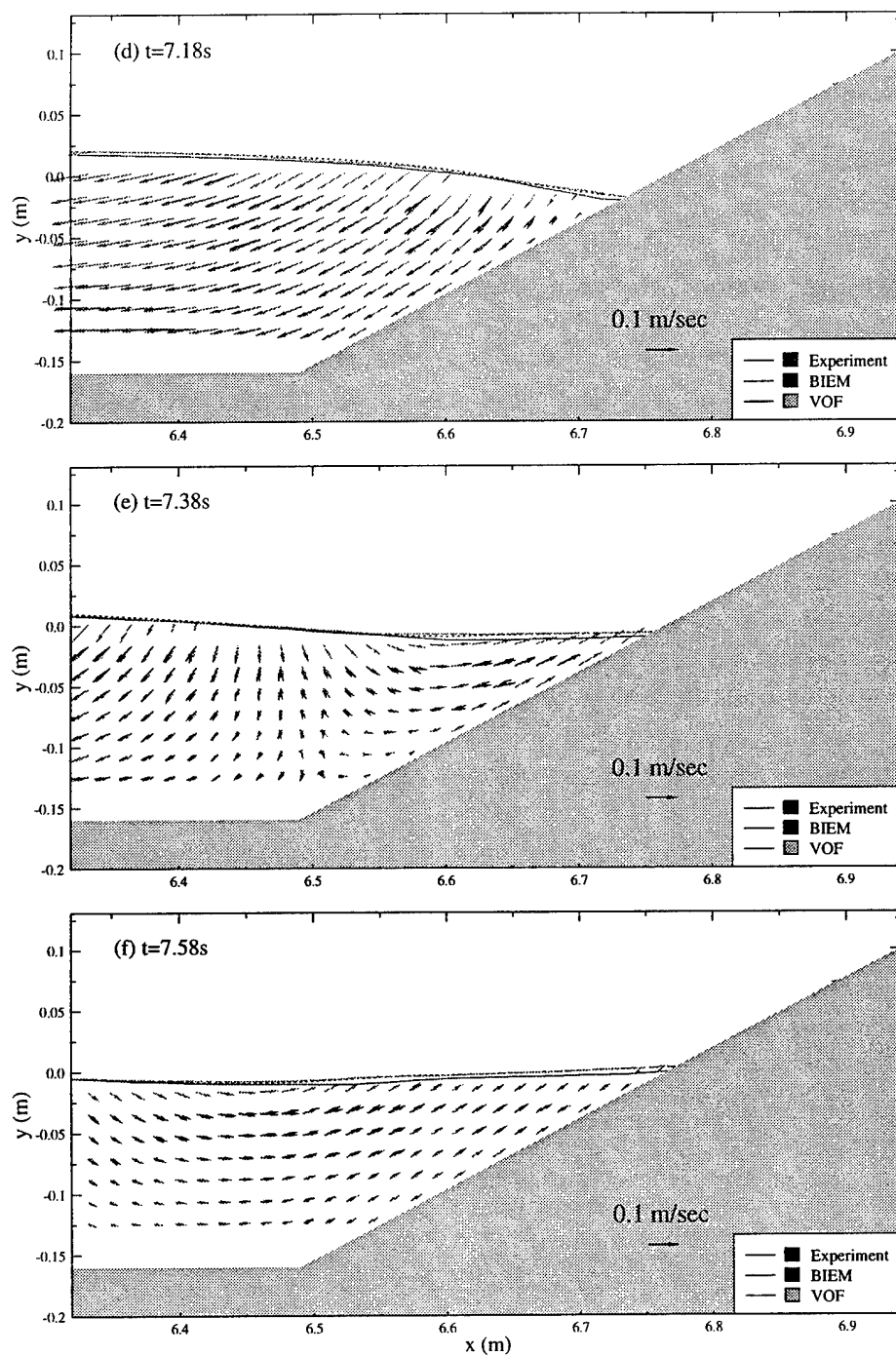Figure 9: Nonbreaking solitary wave runup on a sloping beach

Figure 9: Nonbreaking solitary wave runup on a sloping beach

of velocity field agrees well only in the rear part of wave. Near the wave front, the discrepancies between experimental data and numerical results are obvious, mainly due to different velocity directions. Such discrepancies imply the existence of phase errors. It is found that the PIV system has a timing error in the range of $0.01s$. Such a small timing error is insignificant normally, considering the wave period is in the order of magnitude of $1s$. However, during the transition from runup to rundown, such an error might becomes crucial because the local time scale for such transition process is in the order of $0.1s$ from the experimental measurements. Thus, we expect the velocity disagreement in the wave front is most likely caused by the timing inaccuracy.

Figure 9(c) ($t = 6.78s$) shows that the wave is running down on the beach and figure 9(d) ($t = 7.18s$) shows that the wave is approaching its maximum running down point. Both the wave profile and velocity field comparisons are satisfactory in these two frames. After wave reaches its maximum rundown point, the positive pressure starts to push it back and forms the secondary runup. Such process is shown in figure 9(d) ($t = 7.38s$) and figure 9(e) ($t = 7.58s$). Small discrepancies again show up in velocity field comparison at $t = 7.38s$ when the wave begins to climb up the slope. Such discrepancies, which is expected to be caused by timing inaccuracy as well as the sensitivity of wave during transition process, is diminishing as time precedes. This can be observed in figure 9(f).

5.4 Breaking Solitary Waves Runup on Beach

In this example, the breaking solitary runup on the beach is simulated. The detailed experimental setup for this testing problem is referred to Synolakis (1986) and Zelt (1991). The important parameters are summarized here. The still water depth varies from $0.21m$ to $0.29m$. The beach slope is $2.88°$ and is about $1/20$. A solitary wave which has a wave height to still water depth ratio of 0.28 was generated. Wave gauges were used to record the free surface displacement during the runup and rundown. In the VOF computation, the computational domain starts from the toe of beach and it is discretized with a 260×65 uniform grid system with $\Delta x = 0.025m$ and $\Delta y = 0.005m$. The time step is automatically adjusted during the computation to satisfy the stability constraints by both advection and diffusion processes, i.e., equations (100) and (101). Similar to the previous nonbreaking solitary wave, both the velocities and free surface displacement are specified on the right boundary based on the analytical solution for solitary wave. Since the $k - \epsilon$ model is employed during the computations, the specification of the inflow boundary conditions for both k and ϵ is necessary. As shown in equation (43), both production term and dissipation term for ϵ become singular when k goes to zero. Thus, in general low levels of k are enforced in the inflow boundary, i.e., $k = \frac{1}{2}U_t^2$ with $U_t = \delta C$ and C the phase velocity of wave in the constant water region. In our computation, δ is chosen to be around 0.003. It is noted, however,

45

the simulation result in the interior region is basically independent of the value of δ as long as it is small enough. The value of ϵ is calculated using equation (21), for example, $\epsilon = C_d \frac{k^2}{\nu_t}$ with $\nu_t = \zeta \nu$. In our computation, ζ is chosen to be 10. Again, the final result is insensitive to the choice of ζ as long as the calculated ϵ on the inflow boundary remains a low level.

Since the water depth varies in the experiment, the results can only be compared after normalization. Following Zelt (1991), the length scale is normalized by the water depth and the time scale is normalized by $\sqrt{g/d}$. Figures 10(a) to 10(h) show the comparisons of experimental data and numerical results in terms of the free surface profile. The whole process of wave breaking, runup, and rundown is provided. The agreement between the simulated wave profiles and experimental data is excellent.

Compared with the numerical results of Zelt (1991) obtained from the Boussinesq equation and with those of Titov and Synolakis (1995) obtained from shallow water equation, our model provides much better prediction, especially during and after wave breaks. Their depth-averaged models tend to predict larger reflection which is not observed in the experiment and our numerical results (Figure 10(d)). The success of the current model is the result of two aspects. First is that our model solves the Reynolds equations directly and thus is free of the assumption for pressure, which could lead to significant errors during and after the wave breaks. Another is that the more elaborated turbulence model, the $k - \epsilon$ model, provides more realistic turbulence simulation which improves the free surface simulation.

In figure 11(a) to 11(h), the magnitudes of the turbulent intensity are plotted. It is observed that, before the wave breaks, the turbulence is mainly concentrated in a very thin layer near the bottom and the quantities of those turbulence is relatively small. At $t\sqrt{g/d} = 15$, wave starts to break and the increasing large turbulence is generated on the front face of wave. The time of breaking predicted by the numerical model is consistent with what suggested by Zelt (1991). In the experiments, the breaking process occurs between $t\sqrt{g/d} = 15$ and $t\sqrt{g/d} = 20$. The turbulence generated near the free surface is left over as the broken wave moves towards to the beach. The residual turbulence quickly transport to the interior region where it starts to dissipate because of the small mean flow velocity gradient. This can be observed from $t\sqrt{g/d} = 20$ and $t\sqrt{g/d} = 25$. As the wave continues to climb to its highest point, the overall turbulence almost disappears ($t\sqrt{g/d} = 45$). The wave then starts to rundown and the turbulence energy begins to increase again due to the backward flow motion. The intensity of turbulence, however, is relatively smaller than that generated by the violent breaking process during the shoaling. This is observed at $t\sqrt{g/d} = 50$.
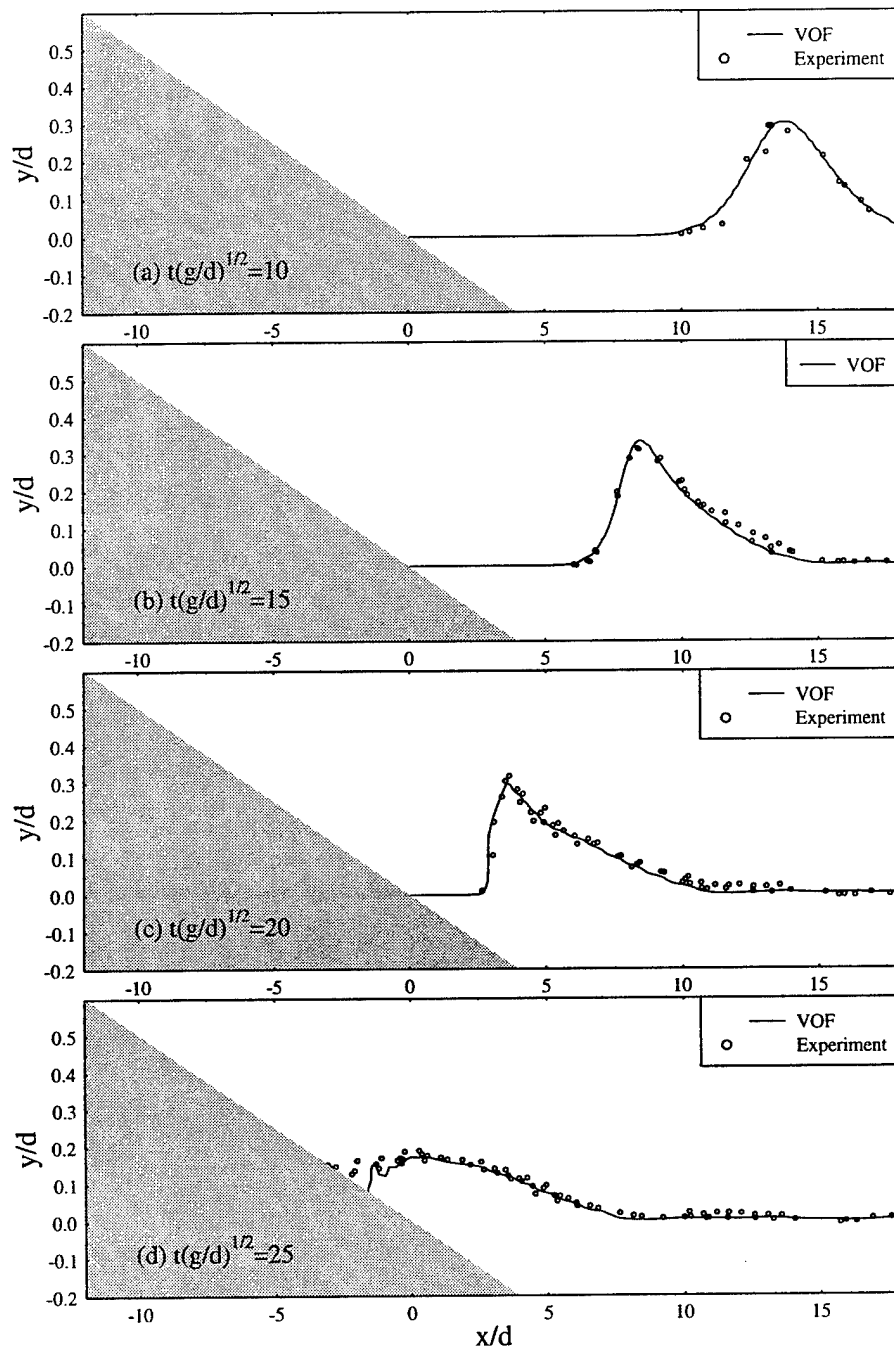
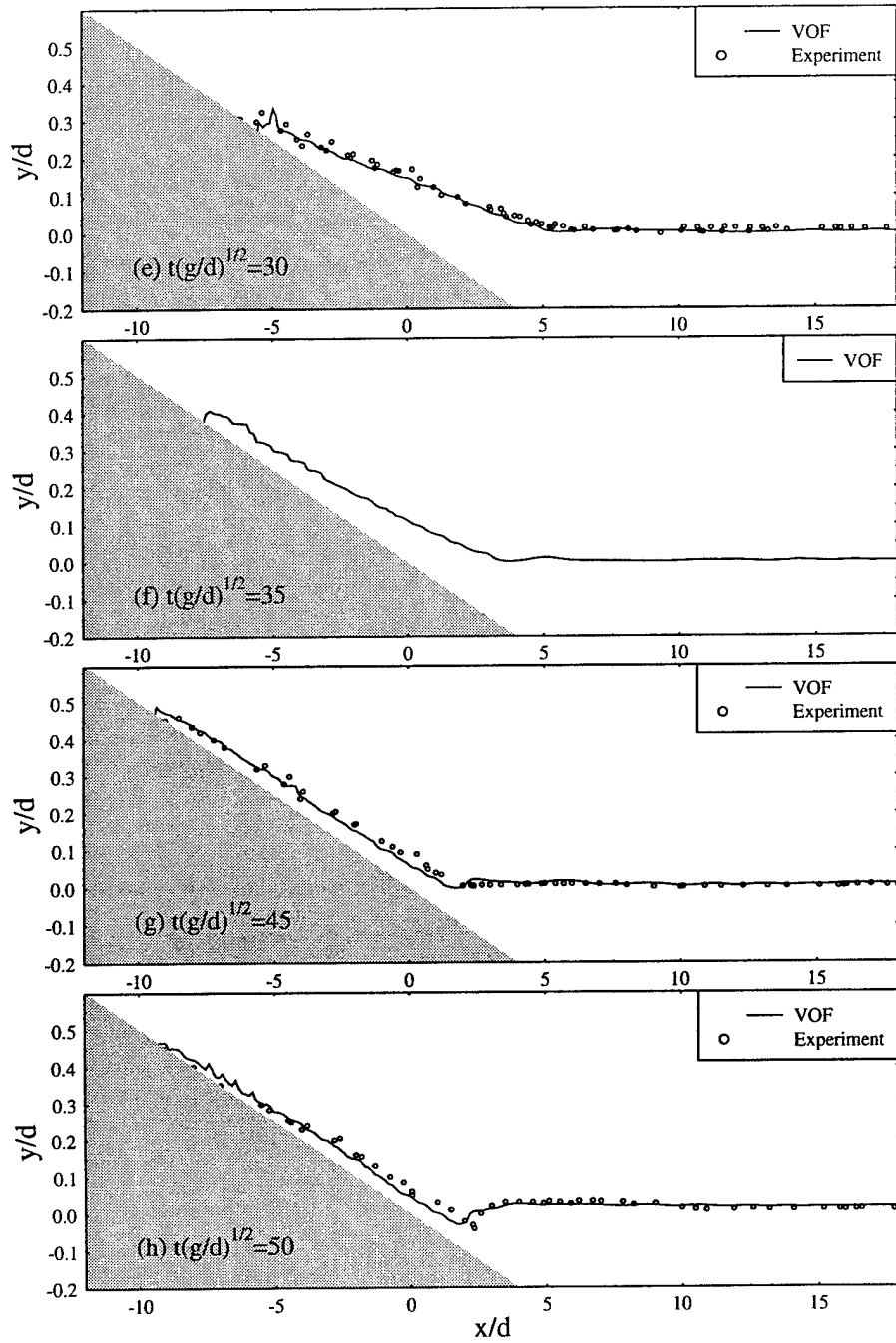Figure 10: Breaking solitary wave runup on a sloping beach

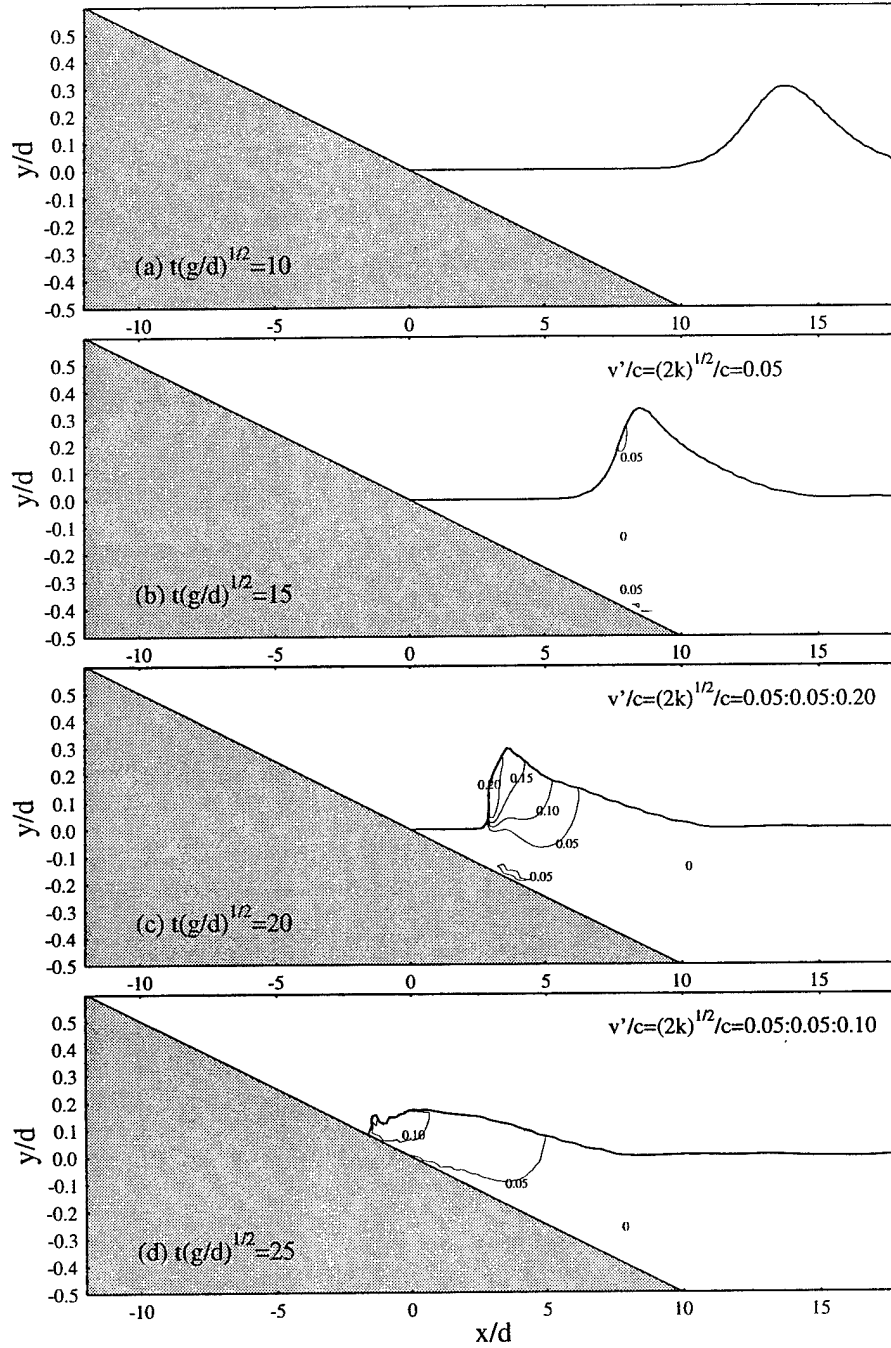Figure 10: Breaking solitary wave runup on a sloping beach

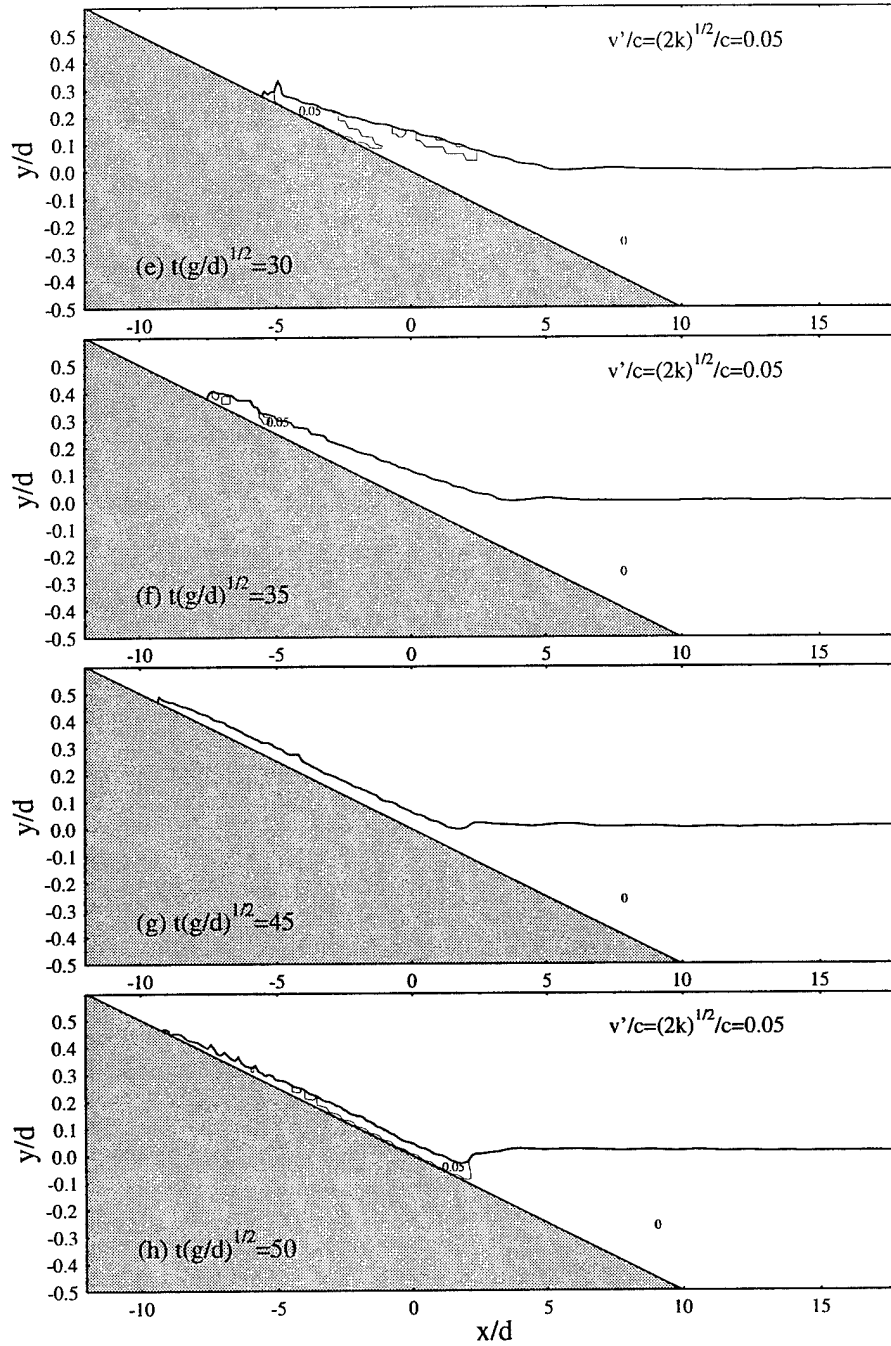Figure 11: Simulated turbulence intensity for breaking solitary wave

Figure 11: Simulated turbulence intensity for breaking solitary wave

6 Conclusions

In this report, we have given a detailed review of the numerical model simulating the breaking wave. The numerical accuracy and the capability of the model is verified by comparing the simulated results with the available analytical solutions and experimental data for both laminar flow and turbulent flow. It is found that for the laminar flow, the model can provide very accurate results. For turbulent flow such as breaking wave, the comparison for the wave profile is excellent. However, the more rigorous validation in terms of turbulence quantities are still needed for a complete verification.

7 Acknowledgments

8 References

Abbott, M. B., Petersen, H. M., and Skovgaard, O. 1978 "On the numerical modeling of short waves in shallow water." *J. of Hydraulic Research*, **16**, no. 3, 173-203.

Abbott, M. B., McCowan, A. D., and Warren, I. R. 1985 "Accuracy of short-wave numerical models." *Journal of Hydraulic Engineering*, **110**, no. 10, 1287-1301.

Adrian, R. J. 1986 "Image shifting technique to resolve directional ambiguity in double-pulsed velocimetry." *Appl. Opt*, **25**, no. 21, 3855-3858.

Battjes, J. A. 1988 "Surf-zone dynamics." *Ann. Rev. Fluid Mech.*, **20**, 257-293.

Chan, K.-C. and Street, R. L. 1970 "A computer study of finite amplitude water wave." *J. of Comp. Phys.*, **6**, 68-94.

Chen, S., Johnson, D. B., and Raad, P. E. 1991 "The surface marker method." *Computational Modeling of Free and Moving Boundary Problems*, **1**, *Fluid Flow*, 223-324, W. de Gruyter, New York.

Chen, S., Johnson, D. B., and Raad, P. E. 1995 "Velocity boundary conditions for the simulation of free surface fluid flow." *J. of Comp. Physics*, **116**, 262-276.

Chorin, A. J. 1968 "Numerical solution of the Navier-Stokes equations." *Math. Comp.*, **22**, 745-762.

Chorin, A. J. 1969 "On the convergence of discrete approximations of the Navier-Stokes equations." *Math. Comp.* **232**, 341-353.

Demuren, A. O. and Sarkar, S. 1993 "Perspective: systematic study of Reynolds stress closure models in the computations of plane channel flows." *J. of Fluids Engineering*, **115**, 5-12.

Harlow, F. H. and Welch, J. E. 1965 "Numerical calculation of time-dependent viscous incompressible flow." *Physics of fluids*, **8**, 2182-2189.

Grilli, S. T., Subramanya, R., Svendsen, L. A., and Veeramony, J. 1994 "Shoaling of Solitary Waves on Plane Beaches." *J. of Waterway, Port, Coastal and Ocean Engineering*, **120**, no. 6, 609-628.

Hirt, C. W. and Nichols, B. D. 1981 "Volume of fluid (VOF) method for dynamics of free boundaries." *J. Comp. Phys.*, **39**, 201-225.

Kobayashi, N. and Karjadi, E. A. 1993 "Documentation of computer program for predicting long wave runup." Research Report No. CACR-93-03, Center for Applied Coastal Research, University of Delaware.

Karambas, Th. V. and Koutitas, C. 1992 "A breaking wave propagation model based on the Boussinesq equations." *Coastal Engineering*, **18**, 1-19.

Kothe, D. B., Mjolsness, R. C., and Torrey, M. D. 1991 "RIPPLE: A computer program for incompressible flows with free surfaces." Los Alamos National Laboratory, LA-12007-MS

Launder, B. E., Morse, A., Rodi, W., and Spalding, D. B. 1972 "Prediction of free shear flows: a comparison of the performance of six turbulence models." *Free Shear Flow*, NASA Conference, 361-426.

Launder, B. E. and Spalding, D. B. 1972 *Mathematical Models of Turbulence.* Academic Press.

Launder, B. E. and Spalding, D. B. 1974 "The numerical computation of turbulent flow." *Computer methods in applied Mech. and Engrg*, **3**, 269-289.

Launder, B. E., Reece, G. T., and Rodi, W. 1975 "Progress in development of a Reynolds stress turbulence closure." *J. Fluid Mech.*, **68**, 537-566.

Lee, J.-J., Skjelbreia, J. E., and Raichlen, F. 1982 "Measurement of velocities in solitary waves." *J. of Waterway, Port, Coastal and Ocean Division*, ASCE, **108**, no. WW2, 200-218.

Lemos, C. M. 1992 "Wave breaking." Springer-Verlag.

Longuet-Higgins, M. S. and Cokelet, E. D. 1976, "The deformation of steep surface waves on water: I. A numerical method of computation." *Proc. R. Soc. Lond.*, **A 350**, 1-26.

Liu, L.-F. P., Yoon, S. B., Seo, S. N., and Cho, Y. 1993 "Numerical Simulation of Tsunami Inundation at Hilo, Hawaii." *Tsunami '93*, Proceedings of IUGG/IOC the International Tsunami Symposium, Wakayama, Japan.

Miyata, H. "Finite-difference simulation of breaking waves." *J. of Comp. Physics*, **65**, 179.

Mizuguchi, M. 1986 "Experimental study on kinematics and dynamics of wave breaking." *Proc. Int. Conf. of Coastal Eng.*, 589-603.

Dommermuth, D. G., Yue, D. K., Lin, W. M., and Rapp, R., J. 1988 "Deep-water plunging breakers: a comparison between potential theory and experiments." *J. Fluid Mech.*, **189**, 423-442.

Nadaoka, K., Hino, M., and Koyano, Y. 1989 "Structure of the turbulent flow field under breaking waves in the surf zone." *J. Fluid Mech.*, **204**, 359-387.

Peregrine, D. H. 1967 "Long waves on a beach." *J. Fluid Mech.*, **27**, no. 4, 815-827.

Raad, P. E., Chen, S., and Johnson, D. B. 1994 "The introduction of micro cells to treat pressure in free surface fluid flow problems." *ASME Winter Annual Meeting*, Chicago, Illinois.

Rodi, W. 1980 "Turbulence Models and Their Application in Hydraulics – A State-of-the-Art Review." I.A.H.R. publication.

Schäffer, H. A., Madsen, P. A., and Deigaard, R. 1993 "A Boussinesq model for waves breaking in shallow water." *Coastal Engineering*, **20**, 185-202.

Skjelbreia, J. E. 1987 "Observation of breaking waves on sloping bottoms by use of laser doppler velocimetry." California Institute of Technology, Report No. KH-R-48.

Stive, M. J. F. 1980 "Velocity and pressure field of spilling breaker." *Proc. 17th Conf. Coastal Engrg*, 547-566.

Svendsen, I. A., Madsen, P. A., and Buhr Hansen, J. 1978, "Wave characteristics in the surf zone." *Proceedings of Coastal Engineering*, 520-539.

Synolakis, C. E. 1986 "The runup of long wave." Ph.D. thesis. California Institute of technology, Pasadena, California.

Ting, F. C. K. and Kirby, J. T. 1994 "Observation of undertow and turbulence in a laboratory surf zone." *Coastal Engineering*, **24**, 51-80.

Ting, F. C. K. and Kirby, J. T. 1995 "Dynamics of surf-zone turbulence in a strong plunging breaker." *Coastal Engineering*, **24**, 177-204.

Ting, F. C. K. and Kirby, J. T. 1996 "Dynamics of surf-zone turbulence in a spilling breaker." *Coastal Engineering*, **27**, 131-160.

Titov, V. V. and Synolakis, C. E. 1995 "Modeling of breaking and nonbreaking long-wave evolution and runup using VTCS-2." *J. of Waterway, Port, Coastal, and Ocean Engineering*, **121**, no. 6, 308-316.

Wang, Y. and Su, T.-C. 1993 "Computation of wave breaking on sloping beach by VOF method." *Proc. of the third Int. Offshore and Polar Engineering Conf.*, 96-101, Singapore.

Zelt, J. A. 1991 "The run-up of nonbreaking and breaking solitary waves." *Coastal Engineering*, **15**, 205-246.